Chapter 8
Photonic Structures for Coloration in the Biological World

Jian Zi, Biqin Dong, Tianrong Zhan, and Xiaohan Liu

Abstract In the biological world the living organisms have exploited photonic structures to produce striking structural coloration since the Cambrian period. In recent years, structural colors and associated photonic structures have received increasing attention from scientists in a wide variety of disciplines ranging from physics, biology, and chemistry to material science. Revealed natural photonic structures are diverse, delicate, and multifunctional as well. Natural photonic structures and their ingenious ways of light steering could be a great source of inspiration, invaluable to our bio-inspired technologies. In this chapter, we will give a review on natural photonic structures and their coloration. A historical survey is given in Sect. 8.2. In Sect. 8.3, we discuss the mechanisms of structural coloration, including interference, diffraction, scattering, or their combination. Experimental and theoretical methods for studying natural photonic structures are briefly reviewed in Sect. 8.4. In Sect. 8.5, we present some typical photonic structures occurring in the biological world, such as thin films, multilayers, diffraction gratings, photonic crystals, and amorphous photonic structures, and also discuss their coloration mechanisms. An outlook is given in the last section.

8.1 Introduction

In the biological world, the evolution of coloration stems from the fact that light could be a significant selection pressure for certain life forms. As a result, colors and also color patterns may have important biological, physical, and even physiological

J. Zi (✉) • B. Dong • T. Zhan • X. Liu
Department of Physics, Key Laboratory of Micro and Nano Photonic Structures (Ministry of Education), and Key Laboratory of Surface Physics, Fudan University, Shanghai 200433, China
e-mail: jzi@fudan.edu.cn; dong_bq@hotmail.com; 071019035@fudan.edu.cn; liuxh@fudan.edu.cn

X.Y. Liu (ed.), *Bioinspiration: From Nano to Micro Scales*, Biological and Medical Physics, Biomedical Engineering, DOI 10.1007/978-1-4614-5372-8_8,

significance. It is thus not surprising that the study of the mechanisms of color production in the biological world attracted the attention of scientific giants like Newton, Michelson, and Lord Rayleigh.

There are several ways to produce coloration in the biological world. The most general cause of coloration is the presence of pigments. Pigments can selectively absorb certain wavelengths of light and reflect or scatter others. Fireflies and many marine organisms can produce coloration by bioluminescence. In bioluminescence, energy will be released in the form of "cold light" emission via chemical reactions. Fluorescence can also generate coloration for materials containing fluorescent molecules when illuminated by ultraviolet (UV) light.

Another important category of color production is structural coloration. Distinctly different from other categories, structural colors are of structural origin, namely, from the interaction of natural light with photonic structures whose feature sizes are comparable to the visible wavelengths. Structural coloration is thus purely produced by physical means via optical phenomena such as interference, diffraction, scattering, or their combination.

Structural colors possess many interesting features that are distinct from pigmentary colors since they are produced structurally. Generally, structural colors are bright and highly saturated, and are hereby called "metallic colors" sometimes. They may display iridescence,[1] i.e., a color change with perspective. Variations in structures or contrast of refractive indices may alter or even destroy structural colors, for instance, by applying pressure or infiltrating liquids into air voids. In contrast to pigmentary colors, structural colors would not fade provided that the associated photonic structures retain unchanged.

In recent years, structural colors and associated photonic structures have been subjected to extensive studies because of their scientific and practical importance [1–9]. Studies of structural colors could offer important information related to their evolution, biological functions, structural formation, and strategies of light steering. On the other hand, structural colors may have potential applications in a variety of industries such as photonics, display, painting, and textile. Natural photonic structures and their ingenious ways of light steering could be a great source of inspiration in our design and fabrication of new optical materials and devices for future technological applications.

8.2 Historical Survey

Historically, Hooke and Newton might be the first ones to give a scientific description of structural colors. In his book *Micrographia* published in 1665, Hooke described his microscopic observations on the feathers of peacock and duck, and

[1]The terms *structural color* and *iridescent color* are sometimes used indiscriminately to name colors produced structurally. An iridescent color is certainly a structural color. But a structural color may not display iridescence.

other feathers of changeable colors. Newton described in his book *Opticks* published in 1704 that the color production mechanism for the finely colored feathers of birds and particularly those of peacock tails is after the same manner of thin films. Both Hooke and Newton attributed feather colors to the thin films of the transparent parts of feathers, but the true physical mechanism was still unanswered.

We now know that the correct mechanisms of structural coloration rely on the wave nature of light, resulting from the interaction of natural light with photonic structures. But quantitative descriptions of reflection, refraction, interference, diffraction, and scattering had to wait until the establishment of the electromagnetic theory by Maxwell in 1873, known as Maxwell's equations.

Ever since the distinction of pigmentary and structural colors, there existed a big debate on the cause of structural coloration in the early twentieth century. Michelson [10] supported strongly the claim proposed by Walter [11] that structural colors are *surface colors* caused from a thin layer of pigments by selective reflection, similar to those from metallic surfaces. The conclusion was based on the similar behavior of polarized light when reflected from iridescent structures and from thin films of aniline dyes. So satisfied with his opinion, he even wrote [10] "it is somewhat surprising to find that the contrary view is still hold by eminent naturalists, and it is hoped that the further evidence here presented may serve to emphasis the distinction between 'metallic' or 'surface' colours and the remaining classes of colours (due to pigment, interference, and diffraction)."

On the opposite side, Lord Rayleigh [12] believed that iridescent colors such as those of peacocks and insects are interference colors from thin films. Many experimental results defied Michelson's suggestion. For example, in *Micrographia* Hooke described the observation that the iridescent colors of peacock feathers would be destroyed by water wetting, and "the colours again appear in their former lustre" by continuous evaporations. Biedermann [13] also noticed that the colors of all iridescent scales of beetles would change after their immersion in liquids, and if the refractive index of a liquid approaches that of chitin, the colors would vanish completely. Besides color changes by liquid infiltrations, Mollock [14] even found that the structural colors of scales or feathers could be destroyed by applying pressure. Merritt [15] might be the first to use spectroscopy to characterize structural colors optically. He measured reflection spectra of pigeon feathers and butterfly wings under different incident angles, and found that reflection minima shifted to a short wavelength with increasing incident angles, which could be explained by thin-film interference. Onslow [16] and Mason [17–21] conducted a multitude of microscopic observations on insect scales and bird feathers, and supported the interference origin of iridescent colors. With convincing arguments, the opinion that iridescent colors are of structural origin prevails eventually.

It is known that the spatial resolution of optical microscopes should be smaller than a half of the visible wavelengths owing to the diffraction limit. As a result, the relations between structural colors and detailed structural features could be determined after the invention of electron microscopy in 1930s since many photonic structures for coloration have submicron feature sizes. With electron microscopy, Frank and Ruska [22] made the first structural observation for the blue feathers of

Pitta maxima, and revealed a spongy structure of keratin in the barbs. Conventionally, two kinds of electron microscopy are frequently used in the characterizations of natural photonic structures: one is scanning electron microscopy (SEM) and the other is transmission electron microscopy (TEM). With the powerful image resolution of SEM and TEM, a wide variety of natural photonic structures have been identified, including single thin films, multilayers, diffraction gratings, two-dimensional (2D) and 3D periodical photonic structures, amorphous photonic structures with only short-range order, or their composites [1–9].

As for the physical mechanisms of structural coloration, early understandings were almost all attributed to the interference of thin films or multilayers due to the lack of structural information. With the development of both structural characterizations and computation algorithms, interesting mechanisms have been uncovered. Structural coloration can thus be understood by interference, diffraction, scattering, or their combination, depending on detailed structural configurations. Despite the great progress in understanding of the mechanisms, there remain still many important questions to be answered in a quantitative way owing to the diversity and complexity of natural photonic structures.

8.3 Mechanisms for Structural Coloration

Different from pigmentary coloration, structural coloration is purely of structural origin, produced by the interaction of natural light with photonic structures via optical phenomena. These optical effects include interference, diffraction, scattering, or their combination.

8.3.1 Interference

The simplest way of structural coloration is thin-film interference [23], as shown schematically in Fig. 8.1a. A soap bubble in sunlight is a known example. As a light beam is incident upon a thin film, it will be reflected and transmitted (refracted) at the upper surface. The transmitted beam at the upper surface will once again be reflected and transmitted when reaching the lower surface. The reflected beam at the lower surface will also encounter reflection and transmission at the upper surface. Due to the different optical path, the reflected light beams at the upper surface possess different phases, eventually leading to interference. The optical path difference between the reflected light beams depends on the refracted angle θ, and the thickness d and refractive index n of the film, given by $2nd\cos\theta$. In calculating the optical path difference, one should consider an abrupt phase change of π when a light beam gets reflected from a low-refractive-index medium to a high-refractive-index medium. This will give rise to an extra contribution $\lambda/2$ to the optical path difference.

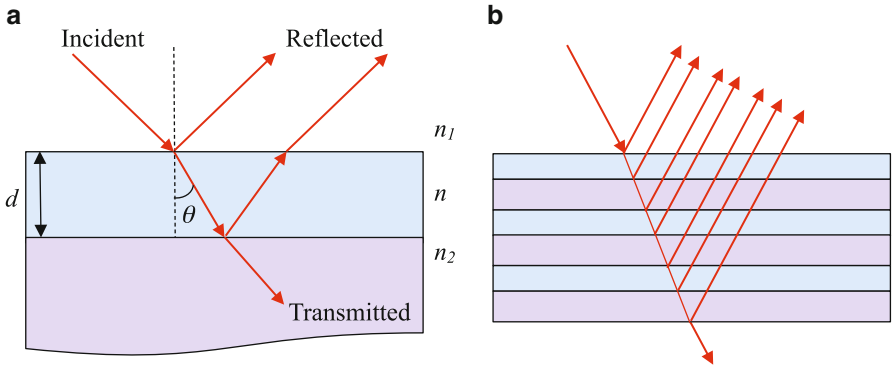

Fig. 8.1 (**a**) Thin-film interference. A thin film with a thickness d and refractive index n is sandwiched between an upper medium with a refractive index n_1 and a lower medium with a refractive index n_2. The refracted angle with respect to the surface normal in the thin film is denoted by θ. (**b**) Interference in a multilayer

Constructive interference occurs when the optical path difference is an integral number of wavelength. On the other hand, destructive interference happens when the optical path difference is a half integral number of wavelength. Considering the possible phase change upon reflection at both the upper and lower surfaces, the condition for constructive interference for $n_1 < n < n_2$ or $n_1 > n > n_2$ is given by

$$2nd\cos\theta = m\lambda, \tag{8.1}$$

where λ is the wavelength in vacuum and m is an integer. For $n_1 < n > n_2$ or $n_1 > n < n_2$, e.g., a free-standing thin film, the condition for constructive interference becomes

$$2nd\cos\theta = \left(m - \frac{1}{2}\right)\lambda. \tag{8.2}$$

For a thin film, its reflection reaches maxima at the wavelengths that satisfy the constructive interference condition, giving rise to structural coloration. It is obvious that the optical path difference increases with increasing incident angle. As a result, reflection peaks undergo a blue shift in wavelength with increasing incident angle, leading to iridescence. Similar to that in thin films, multiple interference occurs also in multilayers, as shown schematically in Fig. 8.1b, since successively reflected light from each interface can interfere with each other.

8.3.2 Diffraction

When light interacts with a periodically structured surface such as a grating shown in Fig. 8.2, diffraction is expected [23]. This is because the scattered light beams by neighboring corrugations possess a constant optical path difference

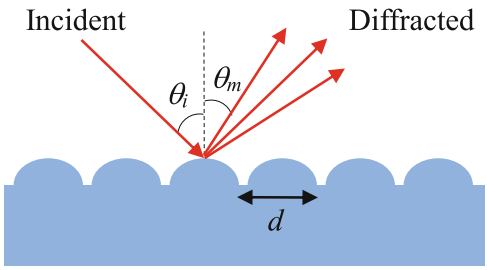

Fig. 8.2 Diffraction by a grating consisting of a periodically corrugated surface. The incident angle is θ_i, the diffracted angle is θ_m, and the grating period is d

$d(\sin\theta_i + \sin\theta_m)$. When this optical path difference is an integral number of wavelengths, i.e., satisfying the following grating equation, diffraction occurs due to the constructive interference of the scattered light beams, namely,

$$d(\sin\theta_i + \sin\theta_m) = m\lambda. \tag{8.3}$$

Here, m is an integer which can be positive or negative, representing the order of diffraction. The zero-order diffraction ($m = 0$) corresponds to the specular reflection. In general, the intensity of nonzero order ($m \neq 0$) diffraction is much smaller than that of the specular reflection.

For a fixed wavelength, diffraction occurs at certain diffracted angles that satisfy the grating equation. For a fixed incident angle, different wavelengths will be diffracted at differently diffracted angles with each order forming a spectrum, leading to structural coloration. For 2D diffraction gratings, structural coloration is also expected due to diffraction, although the grating equation is different from that for 1D gratings.

8.3.3 Scattering

Light will be scattered when encountering irregularities (scatters), e.g., particles. Light scattering depends strongly on light wavelength and scatter geometry and arrangement. In general, light scattering can be classified into incoherent or coherent scattering.

Rayleigh scattering [24] and Tyndall scattering [25] are typical incoherent scattering by single particles. Rayleigh scattering is the light scattering by molecules or particles whose sizes are much smaller than light wavelengths. In Rayleigh scattering, the intensity of scattered light varies inversely as the fourth power of wavelength and shows a strong angle dependence as $(1 + \cos^2\theta)$, where θ is the scattering angle. The blue color of sky is caused by Rayleigh scattering from molecules since short-wavelength light such as violet and blue is scattered much more than long-wavelength light such as yellow and red.

For particle sizes comparable to light wavelengths, it belongs to Tyndall scattering which is much more intense than Rayleigh scattering. Unlike Rayleigh

scattering, there are no simple mathematic formulae for Tyndall scattering. But for spherical particles, light scattering can be mathematically treated by Mie theory [26]. Light scattering by spherical particles is commonly called Mie scattering.

Whether light scattering is coherence or incoherence depends on the coherent length of illumination light and the scatter arrangement as well. For natural light such as sunlight, its coherent length is about a few microns. When the separations of scatters are larger than the coherent length, it can be considered as incoherent scattering. In contrast, if the separations of scatters are smaller than the coherent length, light scattering is coherent since scattered light may interfere with each other.

8.3.4 The Combination

For thin films, multilayers, and diffraction gratings, their coloration can be understood simply by interference or diffraction. In the biological world, there exist many nontrivial photonic structures, e.g., 2D and 3D periodic photonic structures [1–9]. Their structural coloration cannot be simply interpreted by interference, diffraction, or scattering alone. Instead, it results from the combination of interference, diffraction, and scattering.

Periodic photonic structures, those with a spatially periodical variation of refractive index, are also called photonic crystals [27–29]. For light interactions with photonic crystals, there may exist scattering by constituent units, diffraction due to the periodic arrangement, and interference among scattered or diffracted light, leading to complicated photonic band structures [29], analogous to those for electrons propagating in crystalline solids. Between photonic bands, there may exist a partial (along a certain direction) or complete (along all directions) photonic bandgap.[2]

For complicated or composite photonic structures, their color production can be generally interpreted by the combination of interference, diffraction, and scattering. The understandings are usually conceptual. This is because the interplay among interference, diffraction, and scattering may considerably complicate our quantitative analyses. It may even result in new optical phenomena. To understand in a quantitative way, numerical simulations by solving Maxwell's equations are needed.

8.4 Methodology for Studying Natural Photonic Structures

Optical, spectral, and structural information are vital for our understandings of structural coloration. Consequently, both macroscopic and microscopic observations on structural colors are essential. To establish the relations between structural

[2] In natural photonic structures, there exist only partial photonic band gaps because refractive-index contrasts among constituent materials are not big enough to open up complete photonic band gaps.

colors and associated microstructures, structural characterizations at the submicron level are needed. To explore the ultimate mechanisms of structural coloration in a quantitative way, numerical simulations are of great importance.

8.4.1 Optical Observations

With a specimen, the first thing is to determine whether a color is a structural color or not. If iridescence is observed, it should be a structural color. But this method cannot be applied to non-iridescent structural colors. Another way is to immerse the specimen into a liquid aiming to observe the change in color. Commonly used liquids include water, ethanol, and glycerin. If a color change occurs, the color should be a structural color. This is because structural coloration is determined by the spatial arrangement of refractive index. Liquid infiltrations into air voids may change this arrangement, leading to a change in color. On the contrary, pigmentary colors do not alter their hue by liquid infiltrations. Structural coloration has an interesting feature that the reflected and transmitted colors are *complementary* provided that the constituents are transparent. This feature can also be adopted to distinguish structural and pigmentary coloration.

Optical characterizations of structural colors are conventionally conducted by optical microscopy under different magnifications. This is because the colored bodies are sometimes too small to be resolved by our naked eye. In some cases, a color perceived by us is a mixed color, resulting from differently colored small bodies which may be resolved with optical microscopy.

For conventional observations, unpolarized light is used. We may also use polarized light to obtain information on polarization effects. For a photonic structure covered with an uneven cortex, glares caused by surface reflection and scattering may hinder our observations. To reduce the glare disturbances, an oil immersion objective can be used. This is because the oil immersion can reduce or even eliminate the refractive-index contrast between oil and specimen, as well as unwanted glares. For certain samples, dark-field microscopy can be used to enhance the topographic contrast of samples.

8.4.2 Spectral Measurements

Spectral characteristics of natural photonic structures can offer important optical information on their structural colors. For spectral measurements, angle-resolved optical spectroscopy is commonly used to obtain angle-dependent reflection, scattering, and even transmission spectra. A typical angle-resolved spectrometer is schematically shown in Fig. 8.3.

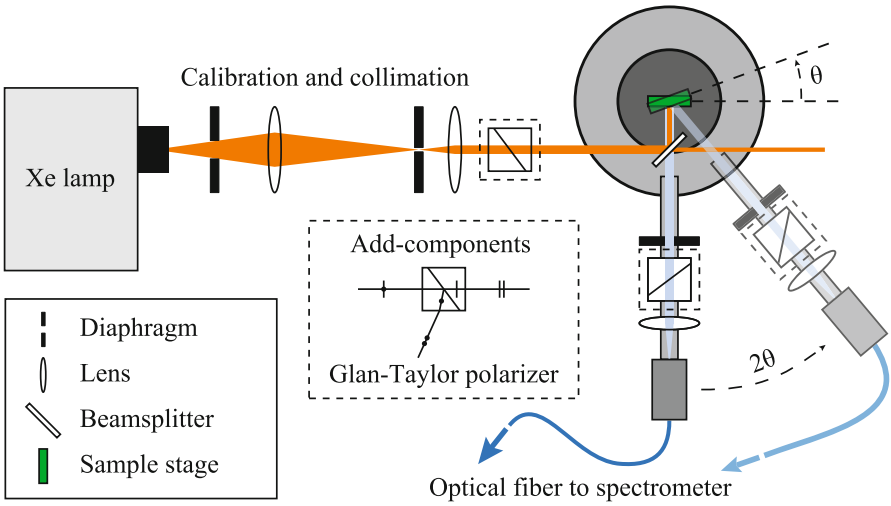

Fig. 8.3 Schematic of a home-built angle-resolved optical spectroscopy at Fudan University. The light source is a Xenon lamp which covers a wavelength range from 250 to 800 nm. Diaphragms are used to control the beam size. A beamsplitter is used to split light beams (50R/50T). Two coaxial motorized rotary stages are used to control the incident and detecting angles. The rotating angles of the upper (*dark gray disk*) and lower (*light gray disk*) stages can be adjusted independently. Samples are placed on the center of the upper stage. An optical fiber is put on the detection arm which is fixed on the lower stage. A high-resolution spectrometer is connected to the fiber. Two Glan–Tailor polarizers can be added in if measurements with polarized light are needed

In this angle-resolved spectrometer, the incident angle θ can be adjusted by rotating the detection arm fixed on the lower stage. Different spectra such as specular reflection (incidence at θ and detection at $-\theta$), scattering (incidence at θ and detection at other angles), backscattering (incidence and detection at the same θ), and transmission can be obtained. Two polarizers can be added in if polarized spectra are to be measured. In measurements of absolute reflectance, a reference standard, e.g., diffuse white, should be used in order to remove the influence of the characteristic wavelength dependence of light sources.

Structurally colored parts of biological samples, e.g., scales of insects and barbules of bird feathers, are usually very small. A single part may even display different structural colors. Under the circumstances, microscopic spectral detections are necessary. A typical microspectrometer that can detect spectra of microscopic regions is schematically shown in Fig. 8.4.

Total reflection, transmission, and absorption spectra can provide important information for structural colors, which can be measured with integrating spheres, as shown in Fig. 8.5. An integrating sphere is a hollow spherical cavity with a diffuse high reflectivity coating on its inner surface, and also with small holes for light entrance and exit. Samples are placed in close proximity to the exit port. Incident light can be introduced, e.g., through an optical fiber. It will bounce around the inner surface and finally impinge the detector.

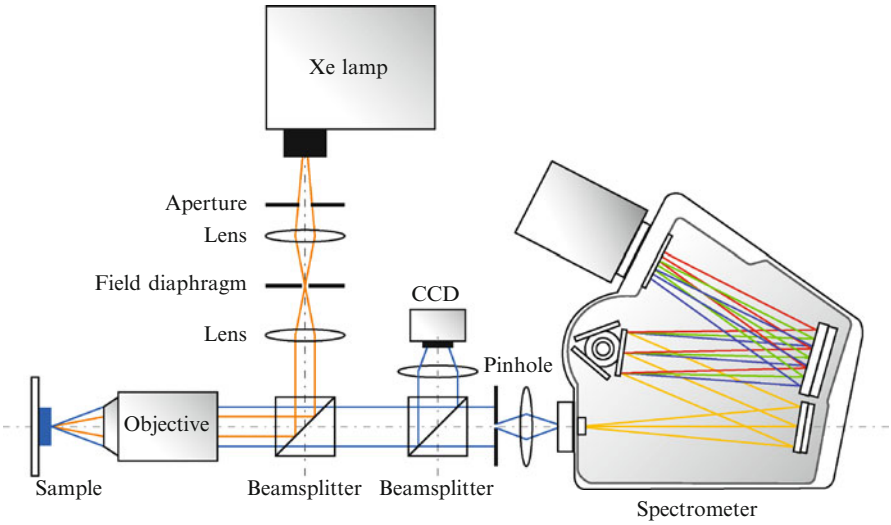

Fig. 8.4 Schematic of a home-built microspectrometer at Fudan University that enables spectral detections of microscopic regions. It is based on an optical microscope with the beam size controlled by the field diaphragm and pinhole

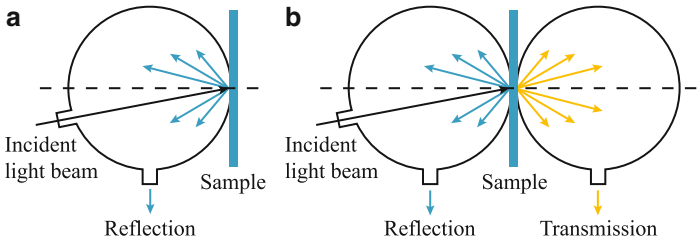

Fig. 8.5 (**a**) Schematic of an integrating sphere for reflection measurements. (**b**) Schematic of a double-integrating sphere for transmission measurements

Transmission measurements require two integrating spheres: one serves as a uniform light source and the other is used to collect transmitted light. Absorptance A can also be obtained, from the formula $A = 1 - R - T$, where R is reflectance and T is transmittance.

8.4.3 Color Specifications

Any possible color can be specified according to their hue, saturation, and brightness. The hue of a color can be considered as the peak wavelength in its reflection spectrum. Saturation tells the purity of the color, characterized by the peak width.

The narrower the peak width is, the higher the saturation is. Brightness renders the relative intensity of the reflection spectrum, strongly related to the response of our vision system.

Practically, colors are specified in color spaces. Commonly used color spaces include CIE XYZ and xyZ color spaces.[3] For the human eye, there are three color-sensitive photoreceptors with sensitivity peaks located in short (420–440 nm), middle (530–540 nm), and long (560–580 nm) wavelengths. Three tristimulus values are thus needed to describe a color since color spaces are 3D.

In the CIE XYZ color space, the tristimulus values are a set of values called X, Y, and Z. For a given illuminating source $D(\lambda)$ and the resulting reflection spectrum $R(\lambda)$ of a color, they can be calculated by

$$\begin{aligned} X &= \frac{1}{k}\int_0^\infty D(\lambda)R(\lambda)\overline{x}(\lambda)\mathrm{d}\lambda, \\ Y &= \frac{1}{k}\int_0^\infty D(\lambda)R(\lambda)\overline{y}(\lambda)\mathrm{d}\lambda, \\ Z &= \frac{1}{k}\int_0^\infty D(\lambda)R(\lambda)\overline{z}(\lambda)\mathrm{d}\lambda, \end{aligned} \tag{8.4}$$

where $\overline{x}(\lambda)$, $\overline{y}(\lambda)$, and $\overline{z}(\lambda)$ are three CIE color matching functions [30] shown in Fig. 8.6a, and $k = \int_0^\infty D(\lambda)\overline{y}(\lambda)\mathrm{d}\lambda$ is a normalization factor which ensures that an object with $R(\lambda) = 1$ yields the component $Y = 1$. In practical calculations, CIE Illuminant D65 [30] is often used as the illuminating source $D(\lambda)$, which matches closely that of the sky daylight.

The CIE 1931 XYZ is at the root of all colorimetry. In the CIE XYZ color space, the Y parameter was deliberately designed as a measure of the brightness of a color. The chromaticity of a color can thus be represented by the two derived parameters x and y, defined by

$$x = \frac{X}{X+Y+Z}, \qquad y = \frac{Y}{X+Y+Z}, \tag{8.5}$$

and derived parameter z can be obtained from $z = Z/(X+Y+Z) = 1-x-y$. The derived color space specified by x, y, and Y is known as the CIE xyY color space which is widely used in practice for color specification. In the CIE xyY color space, the brightness of a color is given by Y, while x and y specify the color chromaticity which can be obtained from the CIE color chromaticity diagram shown in Fig. 8.6b.

[3]The CIE XYZ color space was one of the first mathematically defined color spaces created, according to the human visual system, by Commission Internationale de l'Eclairage (CIE) in 1931.

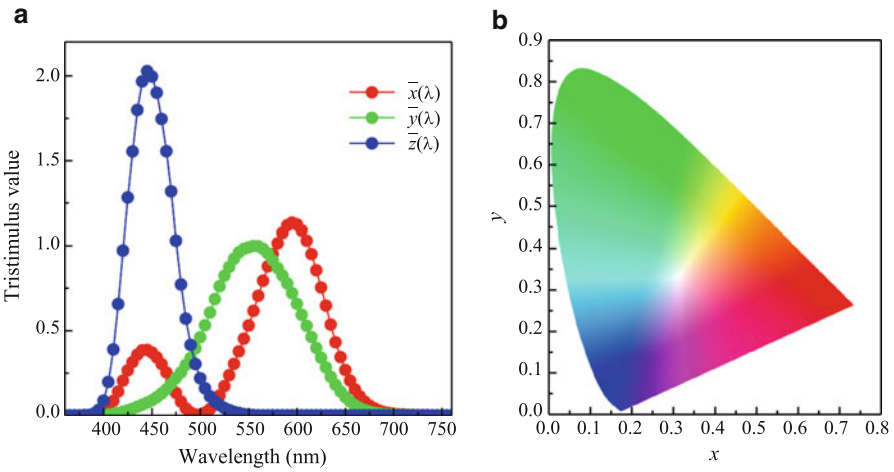

Fig. 8.6 (**a**) CIE 1964 10° color matching functions. (**b**) CIE 1931 2° color space chromaticity diagram. The outer curved boundary is the spectral locus which corresponds to monochromatic light. The straight edge at the lower part represents the line of purples which have no counterparts in monochromatic light. Mixed or less saturated colors appear in the interior with white at the point $(x, y) = (1/3, 1/3)$

8.4.4 Structural Characterizations

Electron microscopes are indispensable tools for structural characterizations because they have a much higher resolving power than optical microscopes. This is due to the fact that electrons have wavelengths much shorter than those of visible light. SEM and TEM are two types of electron microscopes commonly used to characterize natural photonic structures. TEM may have a resolution of atomic level, while the resolution of SEM is poorer by about an order of magnitude than that of TEM.

SEM can image the surface topography of a sample by scanning the surface with a fine high-energy electron beam and measuring reflected electrons. For many samples, structural information on the substructure is needed. This can be done by sectioning the samples. In SEM observations, a thin conductive layer of a few nanometers (gold, platinum, tungsten, or graphite) is usually introduced on sample surfaces in order to produce high topographic contrast and resolution.

Unlike SEM, TEM images samples by taking advantage of transmitted electrons. This means that samples should be ultrathin in order to allow the transmission of electrons. The ultrastructure or even the composition of samples may be distinguished from the intensity of transmitted electrons.

Atomic force microscopy (AFM) can have a spatial resolution at the nanometer scale and can also be used to scan the surface of a sample. AFM relies on a cantilever with a sharp tip and a feedback mechanism that adjusts the tip-to-sample distance

in order to maintain a constant force between the tip and the sample. Due to its working mechanism, AFM has a limited applicability in natural photonic structures as the structural information beneath the sample surface cannot be probed.

8.4.5 Theoretical Treatments

For natural photonic structures, analytical treatments are only possible for some particular cases, e.g., thin films [23]. To give a quantitative description of the optical properties for nontrivial natural photonic structures, numerical simulations are needed. Analytical and numerical results can provide reflection, scattering, transmission, and absorption spectra which can be directly compared with experimental results. Other optical quantities, such as photonic band structures and photon density of states, can be also obtained. With these results, we may uncover interesting mechanisms of structural coloration, light steering strategies, and even new optical phenomena.

With the development of computational algorithms and computer itself, various computational methods have been proposed and implemented to solve Maxwell's equations numerically. Commonly used methods include transfer matrix method (TMM) [31–33], finite-difference time-domain (FDTD) method [34, 35], and plane-wave expansion (PWE) method [29].

TMM was originally developed for multilayers. In TMM, the fields of the adjacent layers are related by a transfer matrix that is composed of two matrices: one is to propagate the fields in a distance in the uniform medium and the other is to make the fields from one side of an interface to the other. From the total transfer matrix, the fields at one side of a multilayer can be related to those at the other side. TMM can be extended to deal with photonic structures of higher dimensions [32, 33].

FDTD is a popular tool which is widely used for electromagnetic computations [35]. The central idea of FDTD is to solve Maxwell's equations based on discretizing time and space into finite grids. The electric and magnetic fields at all points within the computational domain can be calculated. FDTD is a versatile and powerful technique which can be applied to complicated photonic structures. But the spatial grid discretizations must be sufficiently fine, which will increase the computational time and computer memory.

For periodic photonic structures, i.e., photonic crystals, their photonic band structures can offer important information in understanding the optical response. PWE is widely used for calculating photonic band structures [29]. Within the framework of PWE, the electric and magnetic fields are expanded by plane waves, and Maxwell's equations are then cast into eigen-problems. By imposing the Bloch theorem, photonic band structures can be obtained by solving eigen-equations. Photonic band structures can also be calculated by other methods such as TMM and FDTD provided that the Bloch theorem is imposed.

In principle, TMM, FDTD, and PWE are applicable to arbitrary photonic structures. For some special cases, e.g., photonic structures consisting of spheres or spherical cylinders, the scattering matrix method based on Korringa–Kohn–Rostoker techniques is much more efficient [36].

8.5 Photonic Structures Occurring in the Biological World

Color-producing photonic structures are widely spread in the biological world [1–9]. With the advancement of characterization tools, more and more interesting natural photonic structures have been revealed, including thin films, multilayers, diffraction gratings, photonic crystals, amorphous photonic structures, and even composite structures. These photonic structures show a great diversity of construction and topology, leading to optical effects that may implement vital biological functions.

8.5.1 Single Thin Film

A single thin film is the simplest structure that can produce structural coloration via thin-film interference. Perceived structural colors are due to the constructive interference of reflected light from the upper and lower surfaces. Thin-film interference will produce a series of harmonic reflection peaks with equal intensity and frequency interval if the refractive index of a thin film is wavelength independent. However, the intensity of the reflection peaks is rather low. For example, for a thin film with a refractive index of 1.5 its maximal reflectance is less than 20% at normal incidence. In contrast, a multilayer can achieve a very high peak reflectance, ideally as high as 100% in principle.

The wings of most insects are mainly composed of two integument layers apposed closely to form a thin membrane. It was found more than 50 years ago that the transparent wings of some houseflies can produce structural colors via thin-film interference [37]. However, the biological significance of the structural colors as well as color patterns caused by reflecting insect wings has been largely disregarded. This might be due to the fact that these colors are simply produced by thin-film interference like soap bubbles, and imaginarily supposed to flash randomly over the wing surfaces.

In a recent paper [38], the structural-color patterns in the transparent wings of small Hymenoptera and Diptera were studied. These extremely thin wings reflect vivid structural-color patterns caused by the wing membranes. The visibility of these color patterns depends strongly on backgrounds, as shown in Fig. 8.7. In a white background, the reflected structural colors and resulting color patterns are faint or even invisible. This is due to the transparency of the wings. Background light can transmit the wings which will overpower the interference colors. In contrast, these colors and color patterns can be easily perceived by any animal with color vision in a

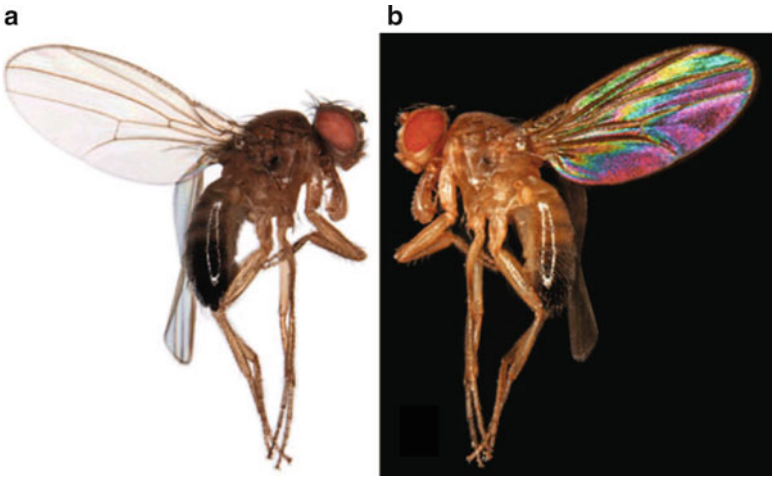

Fig. 8.7 Male *Drosophila melanogaster* on *white* (**a**) and *black* (**b**) backgrounds. (Reproduced from [38])

black background (eliminating the disturbance of reflected light from backgrounds) since about 20% of incoming light can be reflected by the wing membranes. The thickness of the wing membranes is about several hundred nanometers, ideal for thin-film interference, and varies with wing positions. As a result, positions with different thicknesses produce different structural colors, giving rise to specific structural-color patterns. The visibility of these color patterns is affected by the way the insects display their wings against backgrounds.

Interestingly, the wings of small Hymenoptera and Diptera almost universally display stable and non-iridescent structural-color patterns that are often taxon-specific [38], as shown in Fig. 8.8. In other words, these color patterns are visible as well as stable over a wide range of perspective angles. The non-iridescence of the wing structural colors can be understood by the surface morphology of the wing membrane. The membrane surface is uneven with corrugations and dense setae. The corrugations and setae may reduce or even eliminate the iridescence. This is because the existence of the corrugations and setae could cause random scattering, leading to non-iridescence over a wide range of viewing angles.

Another example of structural coloration caused by a single thin film is the iridescent neck feathers of domestic pigeons (*Columba livia domestica*). In spite of a long study history [15,39,40], the detailed origin of their structural coloration was uncovered until recently [41–43]. Basically, there are two kinds of iridescent neck feathers: one is green and the other is purple under normal perspective, as shown in Fig. 8.9. Like many other bird feathers, each iridescent neck feather consists of a central rachis with an array of barbs projecting on both sides. On each side of a barb there is an array of barbules. Each barbule is composed of successively connected segments. The perceived iridescent green and purple colors arise from barbules. Barbs do not possess any iridescent color.

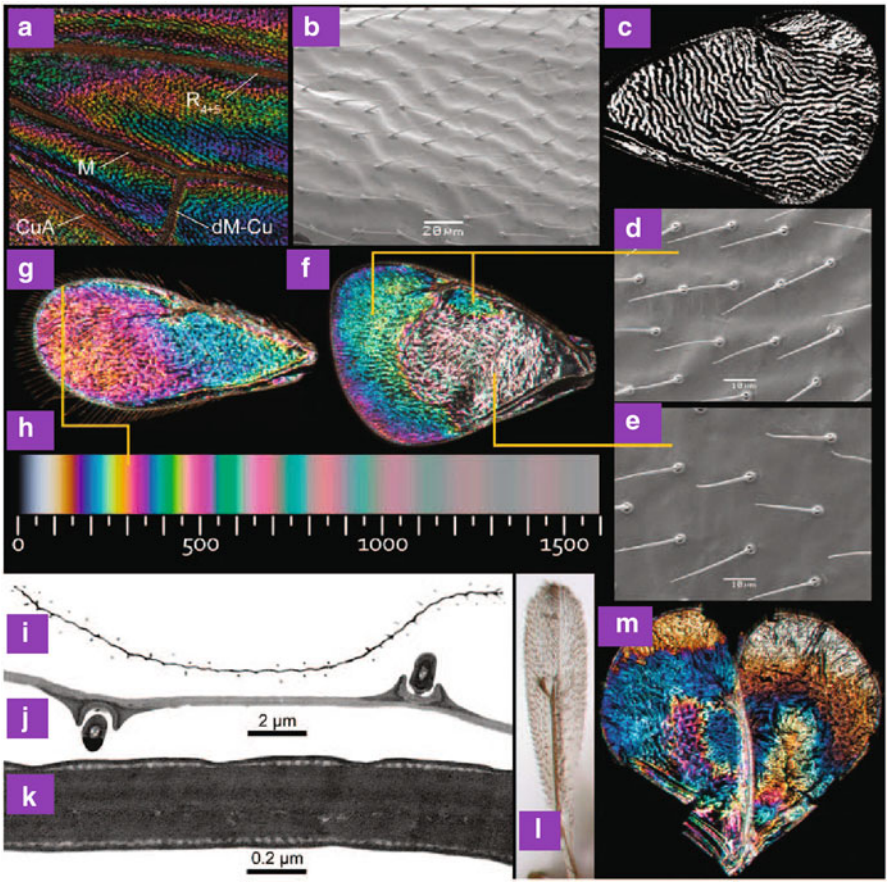

Fig. 8.8 Color and structural features of the wings in small chalcidoid wasps and *Drosophila* showing strong non-iridescent structural-color patterns. (**a**) Midsection of the wing of *D. melanogaster*. (**b**) SEM image of the forewing of *Chrysocharis* sp. (**c**) Duotone image of (**b**). (**d**)–(**f**) Forewing of a male *Achrysocharoides latreillei*. SEM images of corrugated parts and smooth central parts are shown in (**d**) and (**e**), respectively. Resulting structural-color patterns are indicated in (**f**). (**g**) Color pattern of female *Asecodes congruens*. (**h**) Calculated structural colors for a thin film with a refractive index of 1.57 in air under normal incidence with scales indicating its thickness in nanometers. (**i**) Composite duotone image of a whole apical cross-section of the forewing of *Achrysocharoides atys*. (**j**) and (**k**) TEM images of cross-sections of the apical part of a forewing from the same species as in (**g**). (**l**) Left "balloon" forewing of male *Omphale* sp. in frontal view. (**m**) Unequal organization of dorsal (*left*) and ventral (*right*) membranes of an opened left forewing of a male *Achrysocharoides platanoidae* (Reproduced from [38])

SEM characterizations revealed that all iridescent barbules are composed of a central medullary layer surrounded by an outer keratin cortex layer. The barbules are about 2∼4 μm in thickness, while the thickness of the medullary layer varies from 1 to 3 μm. The medulla consists of randomly dispersed melanin granules in

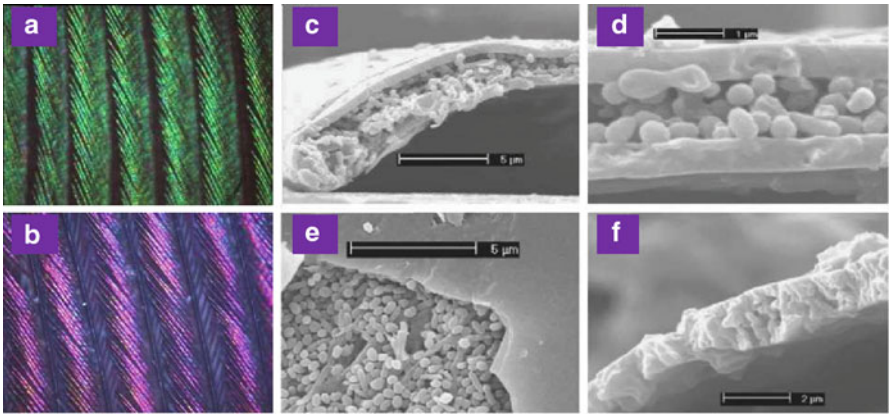

Fig. 8.9 (**a**) and (**b**) Optical microscopic images of iridescent green and purple neck feathers of domestic pigeons under 100× magnification, respectively. (**c**)–(**f**) SEM images of iridescent barbules. (**c**) Perspective view of the cross-section of a green barbule. (**d**) Transverse cross-section of a purple barbule. (**e**) Perspective top view of a green barbule with the top keratin cortex layer removed (lower left corner). (**f**) Perspective view of the cross-section of a gray barbule. Scale bars: (**c**) and (**e**) 5 μm; (**d**) 1 μm; and (**f**) 2 μm (Reproduced from [41])

shapes of spheres, ellipses, and rods, and also a small amount of randomly dispersed keratin. The outer surface of the keratin cortex is rather smooth. Green and purple barbules show different thicknesses. For green barbules, the mean thickness is about 595 nm, while it is about 530 nm for purple barbules. Different from the iridescent barbules, gray barbules are a single uneven layer composed of randomly dispersed keratin and melanin granules, leading to gray colors.

The iridescent neck feathers of domestic pigeons display interesting *opposite* iridescence. Namely, green feathers become purple with the observing angle varying from normal to oblique, while simultaneously purple feathers become green. This can be clearly seen from the measured reflection spectra for iridescent neck feathers at different incident angles, shown in Fig. 8.10. Under normal incidence, iridescent green feathers display a series of harmonic reflection peaks, positioned at about 415, 530, and 730 nm, corresponding to violet, green, and red colors, respectively. With increasing incident angle, all reflection peaks show a blue shift to a shorter wavelength. The violet reflection peak at normal incidence shifts to UV, the green reflection peak to blue, and the red reflection peak to orange. These harmonic reflection peaks can be easily understood by thin-film interference. Although there are two cortex layers, only the dorsal cortex layer gives rise to structural coloration. This is due to the fact that the central layer sandwiched by the two cortex layers is composed of randomly dispersed melanin particles such that light will be absorbed or randomly scattered by this layer. It can also be confirmed by the fact that no colors can be seen if the dorsal cortex layer is removed. Therefore, the central layer

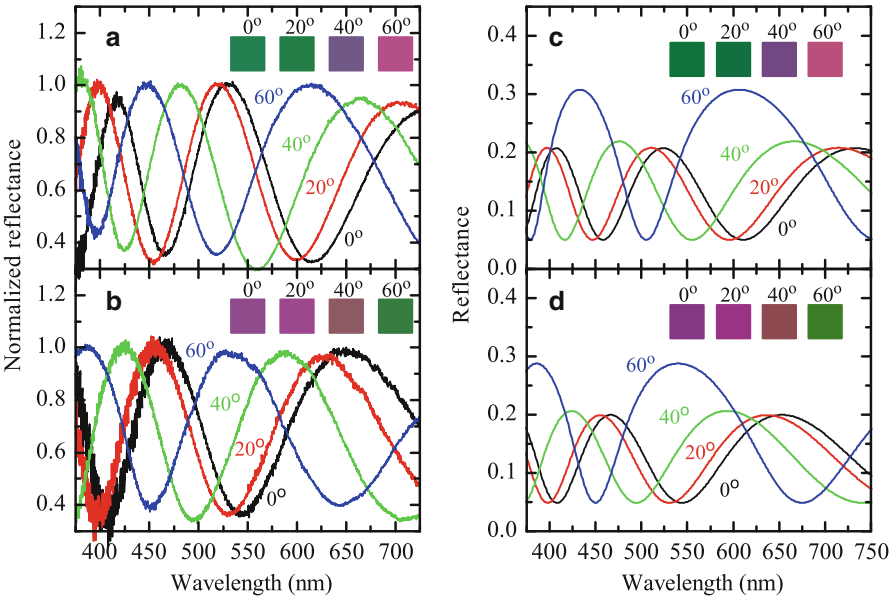

Fig. 8.10 Measured and predicted reflection spectra of iridescent neck feathers of domestic pigeons for unpolarized light at different incident angles. (**a**) and (**b**) Normalized measured results for green and purple feathers, respectively. (**c**) and (**d**) Predicted results for a thin film with a thickness of 595 and 530 nm mimicking green and purple barbules, respectively. The converted RGB colors from the reflection spectra at different incident angles are shown in insets (Reproduced from [41])

plays a role of a poor mirror.[4] As a result, the observed reflectance R should result from the interference in the dorsal cortex layer combined with the reflection from the poor mirror, namely,

$$R = R_1 + (1 - R_1)R_2(1 - R_1), \tag{8.6}$$

where R_1 is the reflectance of the dorsal cortex alone and R_2 is the reflectance of the poor mirror. From experiments, we can determine $R_2 \sim 5\%$ by measuring the region in a barbule where the dorsal cortex layer is removed.

For a thin film in air, its reflectance is given by [23]

$$R_1 = \frac{4r^2 \sin^2\left(2\pi d\sqrt{n^2 - \sin^2\theta}/\lambda\right)}{(1 - r^2)^2 + 4r^2 \sin^2\left(2\pi d\sqrt{n^2 - \sin^2\theta}/\lambda\right)}, \tag{8.7}$$

[4]The central layer may not completely absorb impinging light, and thus acts as a poor mirror with a very low reflectivity.

where λ is wavelength in vacuum, θ is the incident angle, d and n are the thickness and refractive index of the thin film, respectively, and r is the reflection coefficient. For s and p polarizations, the reflection coefficients r are different, given by

$$r_s = \frac{\cos\theta - \sqrt{n^2 - \sin^2\theta}}{\cos\theta + \sqrt{n^2 - \sin^2\theta}}, \qquad r_p = \frac{n^2\cos\theta - \sqrt{n^2 - \sin^2\theta}}{n^2\cos\theta + \sqrt{n^2 - \sin^2\theta}}. \tag{8.8}$$

For unpolarized light, the reflectance of a thin film is the superposition of those from both s and p polarizations, namely, $R_1 = (R_{1s} + R_{1p})/2$, where R_{1s} and R_{1p} are the reflectance for s and p polarizations, respectively.

For a keratin thin film with a refractive index of 1.54 and a thickness of 595 and 530 nm, mimicking respectively the green and purple barbules, the calculated reflection spectra for unpolarized light at different incident angles, obtained from the above equations, are in good agreement with the measured ones. The converted RGB colors from the measured and calculated reflection spectra, shown in the insets of Fig. 8.10, can well reproduce the observed opposite iridescence: green feathers change their coloration from green to purple with the viewing angle varying from normal to oblique, while purple feathers alter their coloration in an opposite way, i.e., from purple to green. This is rather meaningful for color vision since both green and purple colors can be perceived no matter what the perspective angle is, or how the green and purple feathers are arranged. This strategy of opposite iridescence may provide an optimal way for signalling and communication. For multilayers, however, it is difficult to achieve such opposite iridescence. It can thus be concluded that the exploitation of a single thin film for iridescent coloration in neck feathers of domestic pigeons might not be accidental.

Another interesting feature is the optical function of the poor mirror. Without the poor mirror underneath, the peak reflectance of the keratin thin film is less than 17%, and the reflection minimum is zero [41]. With the introduction of the poor mirror, the peak reflectance increases to 20%, and the reflection minimum also increases to about 5%. The poor mirror can thus raise the overall reflectance. Without this poor mirror it is difficult to perceive the iridescent colors in a white background, similar to the case for insect wings [38]. With the poor mirror the color visibility can be largely enhanced since the poor mirror acts also as a black background.

8.5.2 Multilayer

Multilayers are those consisting of alternating layers of materials with different refractive indices. For multilayers, the mechanism of structural coloration is basically similar to that for single thin films, namely, thin-film interference. In general, structural colors produced by multilayers are much brighter than those by single thin films. This is due to multiple interference from the successive interfaces. Multilayers are the most common form of structural coloration in the biological world, appearing, e.g., in insects, fishes, and even plants [7–9, 44–46].

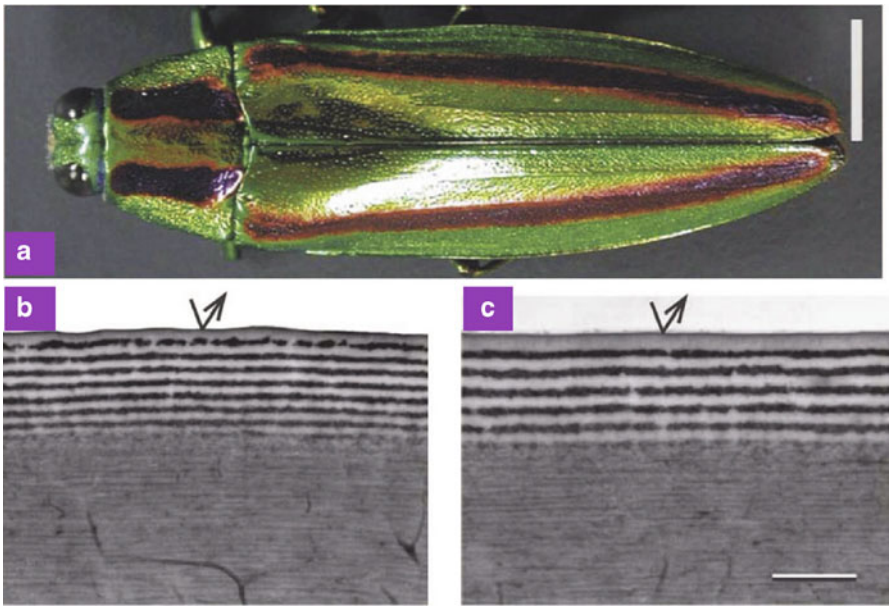

Fig. 8.11 (**a**) Dorsal view of a female Japanese jewel beetle *C. fulgidissima*. (**b**) and (**c**) TEM images of green and purple sections of the beetle elytra, respectively. Scale bars: (**a**) 0.5 cm; and (**b**) and (**c**) 1 μm (Reproduced from [50])

The elytra of some beetles, e.g., the jewel beetles [21], display brilliant, metallic structural colors which are caused by a multilayer in the cuticle. For the buprestid beetle *Euchroma gigantea*, Durrer and Villinger [47] examined its elytra by TEM and revealed an epicuticle multilayer consisting of five melanin layers with a thickness of 60–80 nm embedded in chitin at a regular distance of 60 nm. This multilayer was found to be the basis of color production of the elytra. Similar multilayers were also found in other Buprestidae, e.g., the jewel beetles *Chrysochroa vittata* [48, 49], *Chrysochroa fulgidissima* [8, 50], and *Chrysochroa raja* [51].

Figure 8.11 shows the Japanese jewel beetle *C. fulgidissima* [50]. The elytra of this beetle are metallic green marked with longitudinal purple stripes. Because of the striking iridescence and beautiful luster, this jewel beetle was used as ornament in ancient Japanese times. TEM characterizations revealed that the epicuticle of the green and purple areas consists of stacks of 16 and 12 layers, respectively. The corresponding period for green and purple areas are 160 and 205 nm, respectively. Simulations revealed that both green and purple colors are created by a multilayer with a surprisingly small gradient refractive-index range of 1.6–1.7. The multilayer in the cuticle exhibits both strong angle and polarization iridescence, which is a known optical property for multilayers. The angle dependence can be understood by the fact that the optical path difference between reflected light at successive interfaces differs at different incident angles, which leads to iridescence.

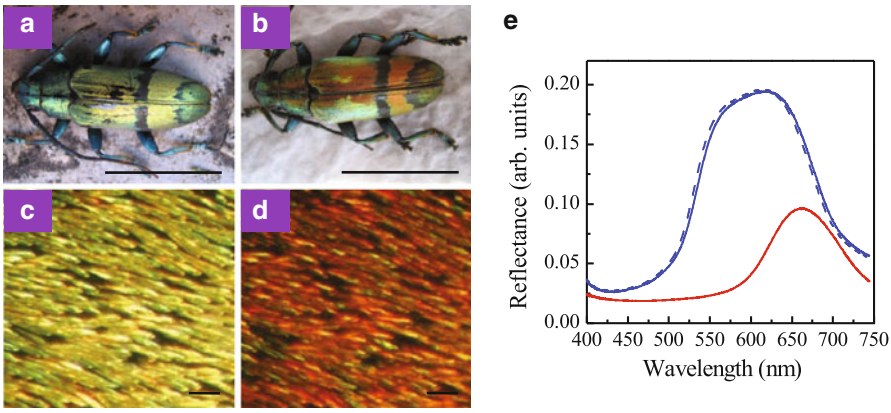

Fig. 8.12 Optical images of the beetle *T. isabellae* in the dry (**a**) and wet (**b**) states. The iridescent golden color in the dry state is able to change to red in the wet state. (**c**) Close-up image of the golden colored region of the elytra in the dry state. In the colored region the elytral surface is densely imbricated with colored scales. (**d**) Same as (**c**) but in the wet state. The color of the scales becomes red. (**e**) Measured reflection spectra of the colored region of the elytra in the dry (*solid blue line*) and fully wet (*solid red line*) under normal incidence. The spectrum for the redried elytra is shown by a *dashed blue line*. Scale bars: (**a**) and (**b**) 10 mm; and (**c**) and (**d**) 100 μm (Reproduced from [53])

Polarization effects, on the other side, can be understood by the fact that *s*- and *p*-polarized light undergoes different reflection and refraction at each interface. Specifically, there exists a brewster's angle for *p* polarization at which reflection is zero.

In addition to cuticles, multilayers also exist in the scales on the elytra of some beetles, e.g., the chaffer beetle *Hoplia coerulea* (Coleoptera) [52]. This beetle belongs to the large family of *Scarabaeidae*. The elytra of the male beetle display a spectacular iridescent blue–violet color. This blue–violet iridescent coloration was found to originate from a multilayer structure in the scales on the elytra. The structure consists of a stack of planar sheets separated by a well-organized network of spacers. It can be approximately viewed as a multilayer. Another example was found in the scale of the beetle *Tmesisternus isabellae* with interesting tunable structural coloration [53].

The beetle *T. isabellae* belong to a large family of longhorn beetles. The colored region of the elytra displays an iridescent golden color in the dry state, as shown in Fig. 8.12. With water dropped onto, the golden color can turn into red within a few minutes. The colored region can recover the golden color by returning to the dry state through evaporation. The colored region of the elytra is composed of long and flat scales, responsible for the metallic golden color. In the dry state the measured reflection spectrum of the colored region is characterized by a broad peak positioned at about 600 nm, showing a golden color. In the wet state, however, the reflection peak is shifted to 662 nm, showing a red color.

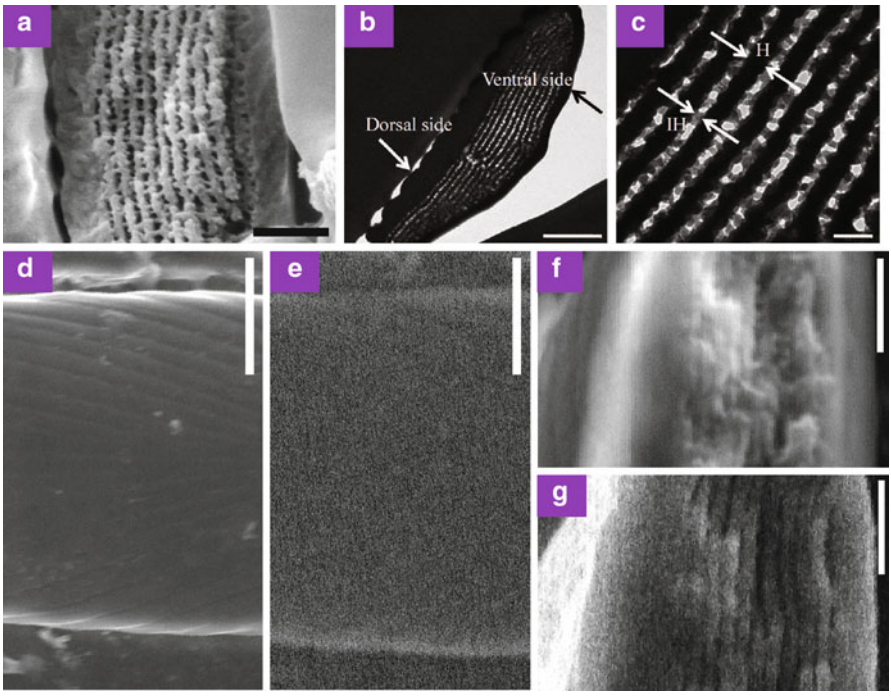

Fig. 8.13 (**a**) Cross-sectional SEM image of a scale of the beetle *T. isabellae* in the dry state. (**b**) and (**c**) Cross-sectional TEM images of a scale in the dry state. (**d**)–(**g**) ESEM images of a scale. (**d**) Top view of the dorsal side in the dry state. (**e**) Top view of the dorsal side in the fully wet state. (**f**) and (**g**) Transverse cross-sections in the dry and fully wet states, respectively. Scale bars: (**a**) 1 μm; (**b**) 2 μm; (**c**) 0.5 μm; (**d**) and (**e**) 5 μm; and (**f**) and (**g**) 1 μm (Reproduced from [53])

The microstructures of the scales in the dry state were characterized by SEM and TEM, as shown in Fig. 8.13a–c. Cross-sectional SEM images revealed a multilayer structure in the interior of the scales. The thickness of the scales is about 3 μm. As seen from both SEM and TEM images, the multilayer is composed of two alternating layers. The first one is a homogeneous layer (dark layers in TEM images) and the second one is an inhomogeneous layer. The inhomogeneous layer consists of nanoparticles (gray areas in TEM images) and air voids (bright areas in TEM images). The number of periods of the multilayer in different regions is different. In the central region of a scale, it is about 10. The thickness of the homogeneous layers is about 105 nm while it is about 70 nm for the inhomogeneous layers.

In order to get insight into the color change of the scales, environmental SEM (ESEM) was used to measure the change in the microstructure of the scales in the wet state, shown in Fig. 8.13d–g. Scales swell noticeably after water absorption. Close-up images show that both the cortex and the multilayer swell in the wet state. The swelling of both the cortex and multilayer is due to the water absorption. The period of the multilayer swells from about 175 nm in the dry state to about 190 nm

in the fully wet state. From cross-sectional ESEM images we can determine that the thickness of the homogeneous layers in the fully wet state swells to about 120 nm, while the thickness of the inhomogeneous layers remains nearly unchanged. The swelling of the period of the multilayer can cause a color change from golden in the dry state to red in the wet state. Furthermore, it could be proved from calculated reflection spectra that the air voids in the wet state are filled with water, since the intensity of reflection in the wet state is much smaller than that in the dry state.

In the biological world, many animals can change their coloration in response to environmental stimuli. The adaptive values of color changes are usually regarded as camouflage, signal communication, conspecific recognition, and reproductive behavior. In principle, color changes can occur via the change in pigment, microstructure, or their combination. Although the precise functionality of the tunable structural coloration in the beetle *T. isabellae* is not clear, the reversible structural color change may certainly render more options for both adaption and function. Owing to its unique properties, tunable structural colors could open new avenue to the applications in display and imaging technology, printing and painting, textile industry, sensing, and photonic devices [54, 55].

In butterflies, there exist also structures closely similar to multilayers which give rise to structural colors. The most significant example may be the *Morpho* butterflies, one of the most representative animals that display brilliant structural colors. In most of the *Morpho* butterflies, the dorsal wings of the male display a brilliant blue color, while their ventral side is usually dark brown in color. Along the direction perpendicular to the wing veins, the blue color shows a weak viewing-angle dependence. Only at large oblique viewing angles the blue color will change rather abruptly to dark blue or violet. Along the direction of the wing veins, however, the blue color will disappear abruptly with increasing viewing angles. This fascinating iridescence in the *Morpho* butterflies has drawn considerable attention of scientists [10, 11, 16, 20, 56–65].

The wings of the *Morpho* butterflies are covered with rows of partially overlapping scales. Various forms of scales are present depending on the species and the wing positions. In the blue iridescent region of the wings, there exist usually two kinds of scales: cover scales (glass scales) and ground scales (basal scales) that lie beneath cover scales. Typical ground scales are rectangular and their dimensions are of the order of 0.1×0.2 mm^2. Figure 8.14 shows a *Morpho* butterfly, *Morpho rhetenor*, its scales, and scale microstructures [60]. The wings of *M. rhetenor* have one layer of highly iridescent ground scales on its dorsal wing surface. The top surface of the ground scales exhibits periodic rows of ridges that extend longitudinally from one end of the scale to the other. Each ridge contains a bookshelf-like multilayer, responsible for the blue structural color. Structural coloration in the wings is determined by many factors such as the geometrical structure of the discrete multilayer and the arrangement of the ridges. The discrete multilayer can produce interference while the ridges and the discrete multilayer itself can give rise to diffraction. As a result, the blue structural color in the *Morpho* butterflies stems from the interplay of interference and diffraction. The parallel ridges can offer a strong anisotropic reflection, while the irregularity in the ridge

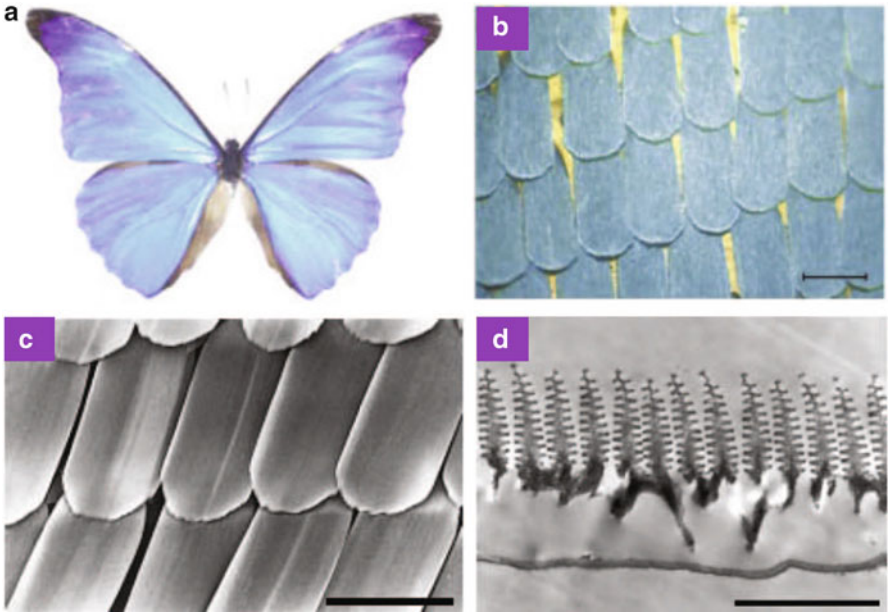

Fig. 8.14 (**a**) Optical image of the butterfly *M. rhetenor*. (**b**) Optical microscopic image of the dorsal wing showing the ordered arrangement of a single layer of ground scales. (**c**) SEM image of the scales. (**d**) Cross-sectional TEM image of an iridescent ground scale. Scale bars: (**b**) 100 μm; (**c**) 120 μm; and (**d**) 3 μm (Reproduced from [60])

height and the small ridge width can eliminate the interference between scattered light from the neighboring ridges, leading to a weak viewing-angle dependence for the blue structural color.

In other butterfly species, e.g., *Ancyluris meliboeus*, similar discrete multilayers were also found, responsible for the wing coloration [66]. These multilayers are highly titled to the base of scales, leading to a strong color flicker contrast from minimal wing movement.

In addition to insects, multilayer structures are also present in spiders. The jumping spider *Cosmophasis umbratica* is a highly ornamented species from Singapore, as shown in Fig. 8.15. Many parts of the male's body are covered with green-orange scales. These scales possess a chitin–air–chitin sandwich structure, which can reflect both the visible and UV light [67]. This spider has an intriguing sexual recognition system that involves the use of UV light. During courtship, the males display their reflecting parts in front of the females. The females tend to accept those males who can reflect more UV light [68].

Although rare, multilayer structures exist also in plants [69–76]. Blue-green iridescent leaves can be usually found in certain understory plants growing in moist and low light environments of tropical rainforests. The first example of a multilayer in plants was found in the leaves of the lycophyte *Selaginella willdenowii* [69, 70].

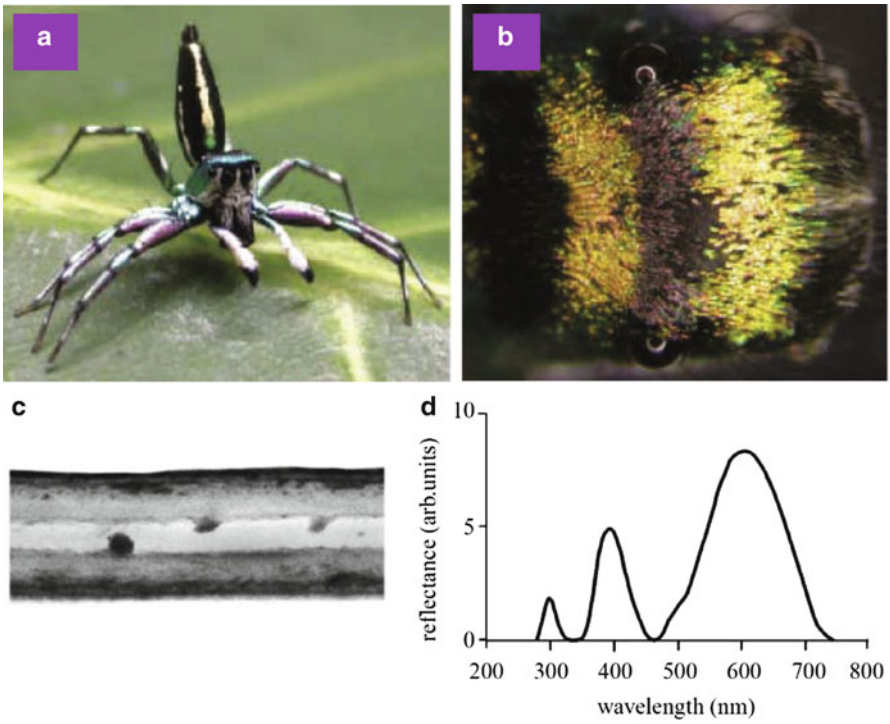

Fig. 8.15 (**a**) Male jumping spider *C. umbratica*. (**b**) Dorsal view of the cephalothorax, showing two bars of green-orange reflecting scales. (**c**) Cross-sectional TEM image of a colored scale, showing a sandwich structure. (**d**) Measured reflection spectrum of the colored scales (Reproduced from [67])

The multilayer in *S. willdenowii* consists of two alternating layers with a period of about 80 nm at the outer cell wall of the adaxial epidermis, producing blue structural coloration. Similar multilayers exist also in the leaves of the Malaysian rain forest understory plants *Diplazium tomentosum*, *Lindsaea lucida*, *Begonia pavonina*, and *Phyllagathis rotundifolia* [72], as shown in Fig. 8.16a–c. Iridescent leaves were also found in the ferns *Danaea nodosa* and *Trichomanes elegans* [71], as well as in the angiosperms *Phyllagathis rotundifolia* and *Begonia pavonina* [72]. In *D. nodosa* there exists a multilayer of cellulose microfibrils in the adaxial cell walls of the adaxial epidermis. In *T. elegans* the blue-green coloration is caused by a multilayer with a remarkably uniform thickness and arrangement of grana in specialized chloroplasts adjacent to the adaxial wall of the adaxial epidermis. In both *B. pavonina* and *P. rotundifolia* the blue-green coloration is caused by a multilayer of parallel lamellae in specialized plastids adjacent to the abaxial wall of the adaxial epidermis.

Multilayer structures were also found in the fruits of *Elaeocarpus angustifolius* and *Delarbrea michiana*, as shown in Fig. 8.16d, producing brilliant blue coloration

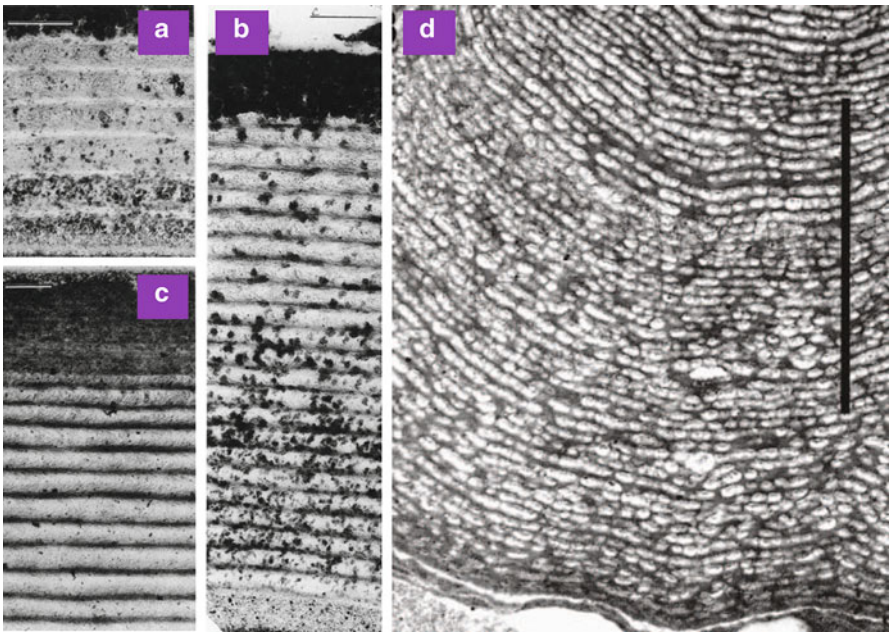

Fig. 8.16 TEM transverse section through helicoidal cell wall in adaxial epidermis of an iridescent green leaf (**a**) and an iridescent blue leaf (**b**) from *D. tomentosu*. (**c**) TEM transverse section through helicoidal cell wall in adaxial epidermis of an iridescent blue-green leaf from *L. lucida*. (**d**) TEM image of the iridisome in the fruits of *D. michieana*, showing an iridescent blue color. Scale bars: (**a**)–(**c**) 0.5 μm; and (**d**) 2 μm ((**a**)–(**c**) Reproduced from [72] and (**d**) from [75])

[74, 75]. The multilayers are so-called "iridisomes" which are within the epidermal cells. The molecular basis of iridosome is primarily cellulose, forming a layered structure that can cause structural coloration via interference.

Structural coloration in plants may have some adaptive benefit, similar to that in animals. Blue coloration in plant leaves may increase the capture of photosynthetically important wavelengths, and may also be exploited as a visual defence against herbivores or as a photoprotective mechanism to protect shade-adapted plants against sun-flecks and other potentially damaging [70]. On the other side, such structural coloration in fruits may aid in attracting mammals and large frugivorous birds, and may also allow ripe fruits to continue photosynthetic carbon assimilation [75].

In addition to simple periodic multilayers in the biological world, there also exist modified multilayers. These modified multilayers include chirped [77–81], chiral [10, 71–73, 82–92], and sculpted multilayers[93–96], which can produce interesting structural coloration and may possess some intriguing selective advantages.

A periodic multilayer is a structure consisting of alternating layers of low- and high-refractive indices (bilayers) with an identical bilayer thickness. In contrast, the bilayer thickness in a chirped multilayer changes progressively with depth.

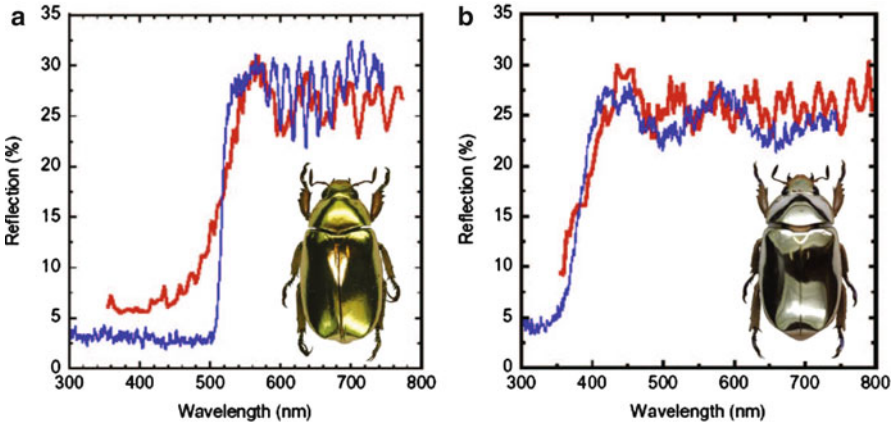

Fig. 8.17 Measured (*blue lines*) and calculated (*red lines*) reflection spectra for *C. aurigans* (**a**) and *C. limbata* (**b**). Calculated results are based on chirped multilayers with linearly decreasing values in the thickness of the sequence of layers (Reproduced from [81])

A periodic multilayer can produce high reflections over a narrow wavelength range.[5] However, a chirped multilayer produces wide-band reflections. This is because for different wavelengths constructive interference occurs for the layers with different *correct* thicknesses, which can result in silvery or golden coloration. For example, certain scarabaeid and tortoise beetles, and lepidopteran larvae and pupae exhibit silvery or golden hues which are caused by chirped multilayers [77].

In the pupaes of the butterflies *Amauris ochlea* and *Euplorea core*, most of their cuticles display a strong metallic golden or silvery luster. Electron microscopic observations revealed a chirped multilayer consisting of up to 250 pairs of bilayers in the exocuticle [78, 79]. The most striking example of metallic golden or silvery coloration may be given by the Coleoptera *Chrysina aurigans* and *Chrysina limbata* [81]. *C. aurigans* displays a brilliant golden color, while *C. limbata* shows a brilliant silvery color, as shown in Fig. 8.17. Chirped multilayers with linearly decreasing values in the thickness of the sequence of layers were assumed, which could result in reflection spectra in good agreement with the measured ones. Metallic silvery coloration is due to a chirped multilayer with constituent layers that can reflect all visible wavelengths. However, in a chirped multilayer without suitable constituent layers that can reflect blue and violet light, metallic golden coloration can be achieved.

Conventional photonic media do not produce circular dichroism. In other words, there is no distinction between left- and right-handed circular polarizations. In contrast, there may exist strong circular dichroism in chiral media. It was shown for the first time by Michelson in 1911 that some scarab beetles can differentially

[5] In other words, the resulting structural color is bright and highly saturated.

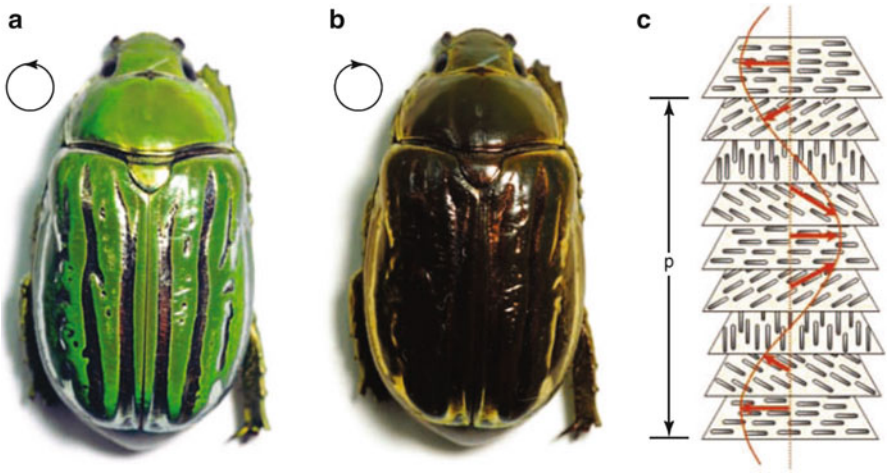

Fig. 8.18 Beetle *C. gloriosa* seen under unpolarized light or with a left-handed circular polarizer (**a**) and with a right-handed circular polarizer (**b**). In (**a**) the bright green color with silvery stripes can be seen. In (**b**) the green color is mostly lost. (**c**) Schematic representation of twisted arrangement of a chiral multilayer structure (Reproduced from [92])

reflect circularly polarized light [10]. The ability to reflect circularly polarized light in certain beetles has attracted considerable attention for nearly a century [82–92]. Ellipsometric measurements confirmed that scarab beetles can reflect predominately the left-handed circular polarization at visible wavelengths. In some cases, however, there is a tendency to reflect the elliptical or right-handed circular polarization at red and near infrared wavelengths [90].

The jeweled beetle *Chrysina gloriosa* possesses a brilliant metallic green color and can reflect selectively the left-handed circularly polarized light [92], as shown in Fig. 8.18. The exocuticle of the beetle consists of many layers of microfibrils aligned parallel with each other, causing a preference for light polarized along the direction of the fibers. Each layer is rotated slightly relative to the layer above, forming a helicoidal stack twisting in the left handedness. This alignment of the layers enables the reflection of the left-handed circularly polarized light, a phenomenon similar to that in cholesteric liquid crystals.

This circularly polarized reflection was also found in some plant species [71–73]. The multilayers found in the outer epidermal cell walls of some iridescent plants produce more elaborate structures, alternating with arcs of cellulose microfibrils. The angle of the cellulose microfibrils changes gradually through the alternating layers up to a total of 180° rotation. The resulting helicoidal structure is remarkably similar to the helical stack of chitin microfibrils, and may be an example of convergent evolution [73].

Most of the multilayers in the biological world take the form of flat layers to produce structural coloration. In flat multilayers, the resulting structural colors are usually very conspicuous and strongly iridescent. However, there exists also a

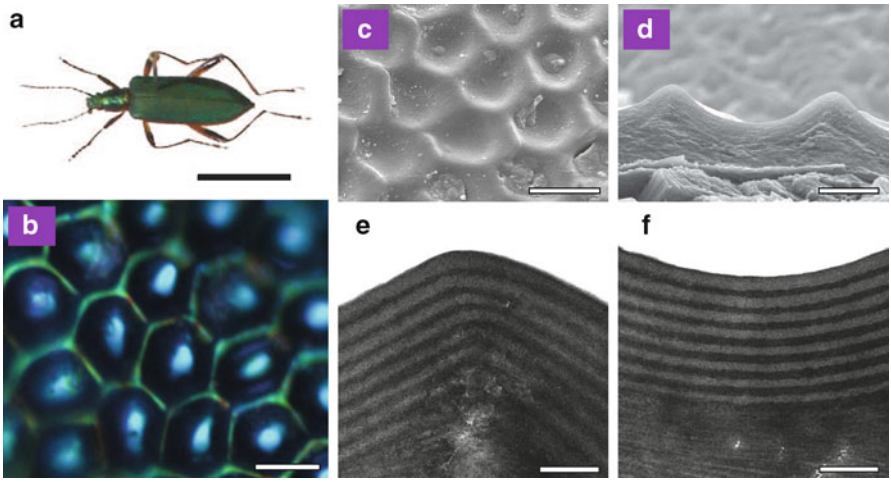

Fig. 8.19 (**a**) Optical image of a male beetle *C. obscuripennis*. Its elytra display an inconspicuous iridescent blueish green color. (**b**) Optical microscopic image of an elytron under 1,000× magnification. (**c**) SEM top view of the outer elytral surface. The elytral surface is composed of an array of hexagonal pits. (**d**) Transverse SEM cross-section of the outermost elytra surface. (**e**) and (**f**) Transverse TEM cross-sections of the ridge and basin regions, respectively. Scale bars: (**a**) 1 cm; (**b**) 5 μm; (**c**) 10 μm; (**d**) 5 μm; and (**e**) and (**f**) 0.5 μm (Reproduced from [96])

special form of multilayers in the biological world, sculpted multilayers [93–95] that can produce structural colors different in many ways from those in flat multilayers, e.g., inconspicuous structural coloration. The adoption of an inconspicuous green color by sculpted multilayers may be more advantageous for camouflage against green backgrounds [94, 95], especially on diffuse leafy surfaces.

Sculpted multilayers found for the first time might be those in the elytra of tiger beetles (Carabidae: Cicindelinae) [93]. The elytral surfaces are in the form of a hexagonal array of pits, and the multilayer in the elytra conforms with the profile of the pits in a sculpted way. The reflecting sculpted multilayer at the basins and ridges possesses different periods and hence cause different structural colors, leading to "pointillistic" color mixing.

A similar sculpted multilayer occurs also in the beetle *Chlorophila obscuripennis* (Coleoptera) [96], as shown in Fig. 8.19. Unlike other beetles, this beetle shows a very inconspicuous iridescent blueish green color. The SEM top-view image shows that the outer surface of the elytra is not flat; instead, it comprises an array of hexagonal pits. Compared with the optical microscopic images, there exists an exact correspondence between the surface morphology and the observed color pattern: the pit ridges produce a green color, the basins a cyan color, and the inclined sides a dull blue color. All these colors change with the viewing angle. From the transverse cross-sectional images, the pits are about 11 μm in size and about 2.8 μm in depth. From TEM images, the sculpted multilayer consists of about 16 thin layers with alternating low and high electron densities, which are the cause of

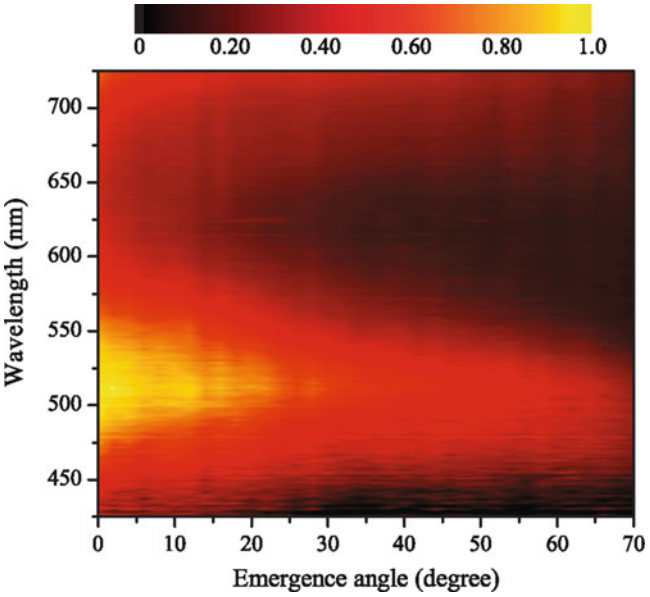

Fig. 8.20 Measured relative emergence intensity for an elytron of the male beetle *C. obscuripennis* as a function of wavelength and emergence angle at normal incidence. The emergence angle is defined as the angle of reflected light with respect to the elytral surface normal. The intensity of non-specular reflection is smaller than that of specular reflection. For normal incidence, non-specular reflection occurs mainly at emergence angles that are smaller than 20°. The intensity of non-specular reflection decreases with increasing emergence angle. At small emergence angles, non-specular reflection is dominant at wavelengths around 520 nm, but at large emergence angels it is dominant at slightly lower wavelengths (Reproduced from [96])

the elytral structural coloration. The layer with low electron density is chitin. By chemical treatments [93], the layer with high electron density was determined to be melanoprotein. The average thickness of both chitin and melanoprotein layers shows distinct differences in different regions. The average thickness of the chitin layer is about 90, 85, and 78 nm at the ridge, the inclined side, and the basin, respectively. For the melanoprotein layer its average thickness in different regions is nearly the same, about 66 nm.

Sculpted multilayers can produce optical effects different from flat ones. In flat multilayers, only specular reflection is expected, leading to conspicuous structural coloration. In contrast, both specular and non-specular reflections exist in sculpted multilayers. Owing to the surface profile, the effective area for specular reflection in a sculpted multilayer is much smaller than that in a flat multilayer. This will lead to inconspicuous structural coloration. In addition to specular reflection, a sculpted multilayer can also render non-specular reflection, giving rise to light emergence at directions of non-specular reflection, as shown in Fig. 8.20. A resulting consequence is that structural coloration can be perceived in a much wider range of viewing angles. This feature may be of significance in signal communication and conspecific recognition.

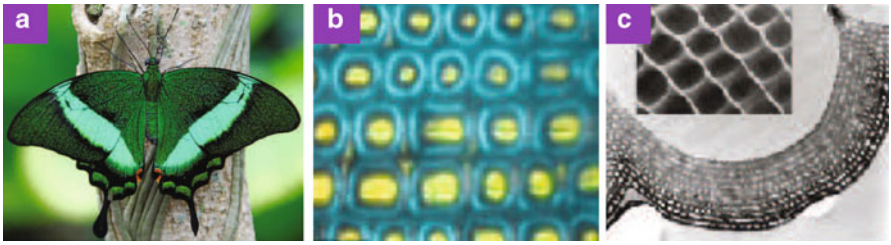

Fig. 8.21 (**a**) Indonesian male butterfly *P. palinurus*. (**b**) Close-up optical image of the surface of a *P. palinurus* iridescent scale, showing the dual-color nature. (**c**) Cross-sectional TEM image showing one concavity on a *P. palinurus* iridescent scale. The inset is the SEM image of the surface of an iridescent scale (Reproduced from [97])

In the wing scales of the Indonesian male butterfly *Papilio palinurus* [97], there also exits a sculpted multilayer, as shown in Fig. 8.21. The bright green coloration of the wing scales is caused by this ingeniously designed sculpted multilayer, which enables the reflection of yellow light at normal incidence from the base of each concavity and blue light through a double reflection from the opposite and perpendicularly inclined sides of each pit, producing a blue annulus with a yellow center. In the beetle *C. obscuripennis* shown in Fig. 8.19, however, the inclined sides produce a dull blue, giving a minor contribution to color mixing. The production of a blue color at the inclined sides in the *P. palinurus* butterfly lies in the double reflection by a pair of orthogonal surfaces inclined about 45° to the scale surface. At normal incidence, reflected light from one inclined surface is directed across to its adjacent inclined side, where it is reflected back to the incident direction. In the beetle *C. obscuripennis*, the inclined angle is, however, much smaller than 45°. Moreover, the pits in the beetle *C. obscuripennis* is hexagonal rather than square in the butterfly *P. palinurus*. As a result, at normal incidence double reflection cannot cause light emergence back to the incidence direction. Nevertheless, at oblique incidence we may still observe a dull structural color produced by the inclined sides (see Fig. 8.19b).

In the Madagascan sunset moth *Chrysiridia rhipheus*, curved multilayers were found showing interesting features [20, 98, 99]. The wings of *C. rhipheus* exhibit a striking iridescent pattern from the arranged scales, as shown in Fig. 8.22. The scales consist of a stack of three to six thin layers and are highly curved from the root to the distal end. Owing to this strong curvature, a valley-like deep grooved structure is present between adjacent two rows of the regularly arranged scales. The combination of the grooved structure and the multilayer gives rise to two different colors: one is the direct reflection from the top flat part of the scales, and the other is the dual reflection between adjacent scales. This color mixing is also strongly polarization-sensitive even under unpolarized illumination, because the reflectivity is naturally different for *s* and *p* polarizations.

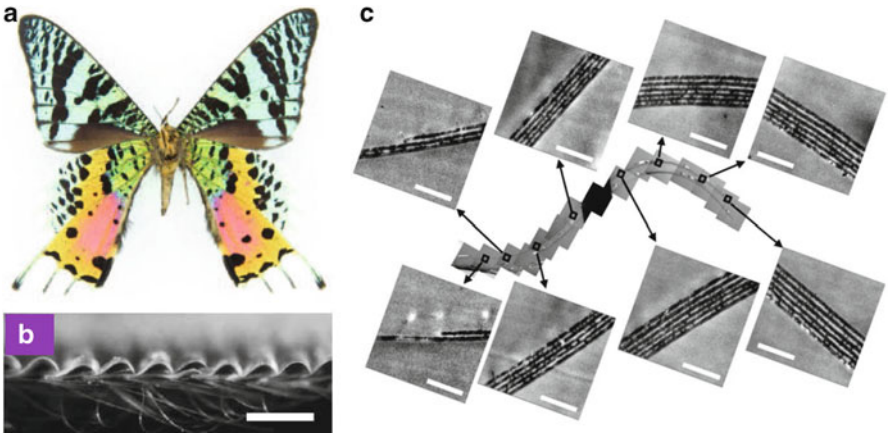

Fig. 8.22 (**a**) Ventral side of a Madagascan sunset moth *C. rhipheus*. (**b**) SEM image of a longitudinal cross-section of the hind wing. (**c**) Cross-sectional TEM image of a cover scale in the longitudinal direction. The enlarged views at various positions are given in the insets. Scale bars: (**b**) 300 μm and (**c**) 2 μm (Reproduced from [98])

8.5.3 Diffraction Grating

Diffraction gratings can generate structural colors by diffraction. In addition to the specular reflection (zero-order diffraction), light can be diffracted at non-specular angles. For natural light, the zero-order diffracted light should be white in color. For a fixed observing angle that differs from the specular one, diffracted light with wavelengths that satisfy the grating equation (8.3) can be perceived. By varying the observing angle, color changes can be seen, leading to iridescence. The ability to disperse spectral light spatially renders diffraction gratings as an indispensable optical element [100]. Diffractive colors and their intensity and spatial distributions depend on many parameters such as the grating period, grating morphology, and refractive index of the grating.

The first revealed biological diffraction grating was probably the one found in 1942 by Anderson and Richards [56] on the elytra of the scarab beetle *Serica sericea*. This dark brown beetle possesses line gratings on its elytra with a period of 800 nm, which can produce brilliant iridescent colors. A taxa list of beetles with cuticular diffraction gratings was described later by Hinton and Gibbs [101–107]. Diffraction gratings are widespread in beetles in 1D as well as 2D forms [46, 108, 109], as shown in Fig. 8.23.

The beetle *Sphaeridiinae gen.* sp. (Hydrophilidae) displays bright diffractive colors caused by an ordered diffraction grating on its elytral surface, as shown in Fig. 8.23a. Up to the third-order diffraction can be clearly seen. The zero-order diffraction is just the specular reflection, showing a bright white appearance. Higher-order diffraction creates interesting rainbow-like spectral colors. Unlike that in the beetle *Sphaeridiinae gen.* sp., the cuticular diffraction grating in the

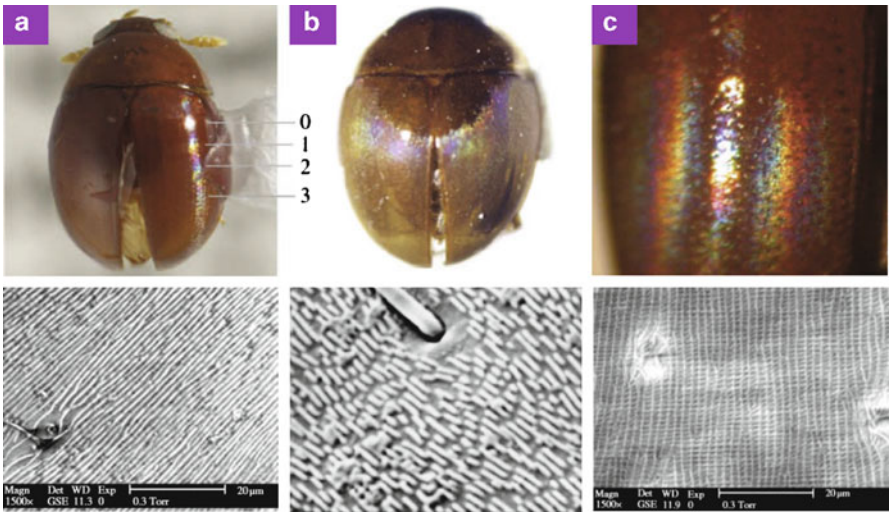

Fig. 8.23 Beetles showing diffractive structural colors (*upper panels*) and corresponding nanostructures of diffraction gratings (*lower panels*). (**a**) Beetle *Sphaeridiinae gen.* sp. and SEM image of the cuticular diffraction grating. Labels indicate the zero-, first-, second-, and third-order diffractive colors. (**b**) Beetle *A. tumerus* and SEM image of the quasi-ordered, discontinuous cuticular diffraction grating. (**c**) Beetle *Pallodes* sp. and SEM image of the 2D cuticular diffraction grating (Reproduced from [46])

beetle *Aglyptinus tumerus* (Leiodidae: Leiodinae) is not very ordered, as shown in Fig. 8.23b. It consists of weakly parallel, discontinuous ridges, but still can diffract incident light and produce structural colors.

In addition to 1D gratings, there also exist 2D diffraction gratings. In a 1D diffraction grating, it cannot diffract light along the direction perpendicular to the grating. In contrast, 2D diffraction gratings can diffract light in all azimuth angles. The beetle *Pallodes* sp. displays a spectral "halo" on its elytra around the point of the specular reflection, which is caused by a 2D cuticular diffraction grating, as shown in Fig. 8.23c.

Some marine animals also use diffraction gratings to produce iridescent colors. One example is the halophores (hairs) on the first antenna of the seed-shrimp *Azygocypridina lowryi* (ostracod) [110], as shown in Fig. 8.24. The halophores possess a diffraction grating with a period of about 600 nm on the surface. The colors on the halophores are caused by this diffraction grating. Different diffraction colors are due to the different orientations of the halophores.

In addition to animals, diffraction gratings also exist in plants, e.g., on the petals of the flowers *Tulipa* sp., *Hibiscus trionum*, and *Mentzelia lindleyi* [111, 112], as shown in Fig. 8.25. In these species, the petal epidermal cells are elongated and flat. In white epidermis, the epidermal cell surface is smooth. In contrast, the pigmented (dark) epidermal cell surface is microscopically uneven, marked with microscopic striations. These striations are nearly periodically arranged, acting as a diffraction

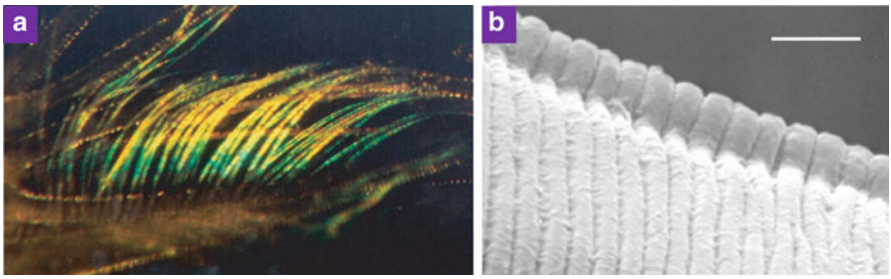

Fig. 8.24 (**a**) Halophores (hairs) on the first antenna of seed-shrimp *A. lowryi* (ostracod). (**b**) SEM image of a diffraction grating on a halophore. Scale bar: (**b**) 2 μm (Reproduced from [4])

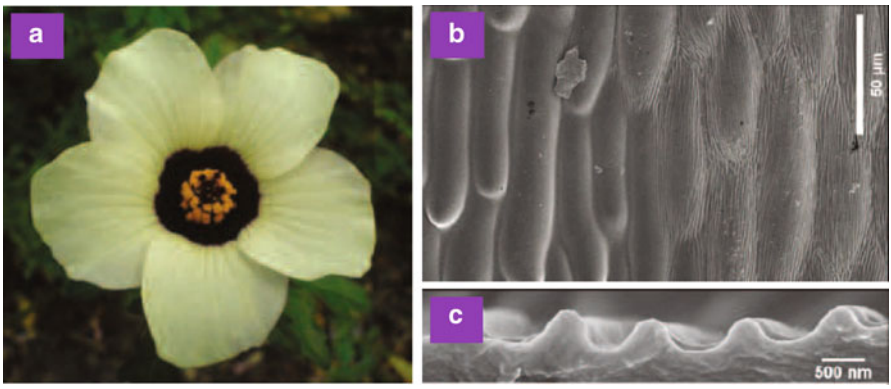

Fig. 8.25 (**a**) Flower *H. trionum*. (**b**) Top-view SEM image of the petal of the flower *H. trionum*. The left-half image corresponds to white epidermis with smooth cells, and the right-half image to dark epidermis (pigmented) with microscopic striations marked on the cell surface. (**c**) Transverse cross-sectional SEM image of the dark epidermis of the flower *T. kolpakowskiana*. The period of the microscopic striations is about 1.2 μm (Reproduced from [111])

grating. These diffraction gratings can diffract light predominantly in UV, which is of great significance for attracting pollinators such as bees and birds.

Another grating structure in plants was found in the edelweiss *Leontopodium nivale* [113]. The whole plane including stems, leaves, and bracts is covered with white hairs consisting of transparent hollow filaments. On the surface of the filaments there exists an array of parallel ridges with a period of about 420 nm. The ridges are about 410 nm in height. This curved diffraction grating can block UV light to reach the cellular tissues underneath since UV light can be strongly absorbed by the filaments, owing to the interplay of diffraction caused by the grating and guiding by the ridges.

Structural coloration produced by diffraction gratings requires that the grating period is comparable to light wavelengths. For wavelengths much larger than the grating period, only zero-order diffraction (specular reflection) exists. These sub-wavelength diffraction gratings can be used as antireflective structures. For example,

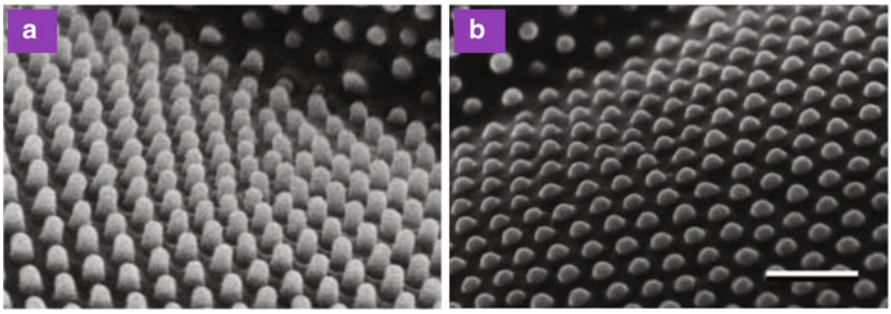

Fig. 8.26 SEM images of the corneal nipple arrays in the nymphalid *Pseudozizeeria maha* (**a**) and the lycaenid *Pseudozizeeria maha* (**b**), showing differences in nipple height and shape. Scale bar: 500 nm (Reproduced from [117])

corneal nipple arrays on the corneal surface of eyes in certain insects function as an antireflective layer [114–116], as shown in Fig. 8.26. Similar structures were also found on the transparent wings of certain insects [117–119], which can increase the transparency of the wings and hence reduce visibility.

8.5.4 Photonic Crystal

Photonic crystals are composite structures with a spatially periodic variation of refractive index [27–29]. As discussed above, light interactions with photonic crystals involve scattering by the constituent units, diffraction by the periodic arrangement of the units, and interference among scattered or diffracted light. Due to the introduced periodicity, light propagation in photonic crystals is strongly modified by the multiple Bragg scattering. As a result, the dispersion relation is characterized by complicated photonic band structures displaying photonic bands and even bandgaps (stop bands). For frequency within photonic bands, light propagation is allowed. For frequency within photonic bandgaps, however, the propagation of light is forbidden. There may exist a complete photonic bandgap for frequency within which light propagations are forbidden for all directions. These interesting features render the control of light propagation by photonic crystals possible, potentially leading to revolutionary approaches in photonics [29].

According to the periodicity in different dimensions, photonic crystals can be classified into 1D, 2D, and 3D. Periodic multilayers are 1D photonic crystals which are already discussed in the previous subsection. Here, our discussions will focus on 2D and 3D photonic crystals in the biological world. As aforementioned, there is no complete photonic bandgap in natural photonic crystals due to the fact that the refractive-index contrast among the constituent materials is not big enough. Only partial photonic bandgaps exist along certain directions. For a photonic crystal with a partial photonic bandgap along a certain direction, light cannot propagate

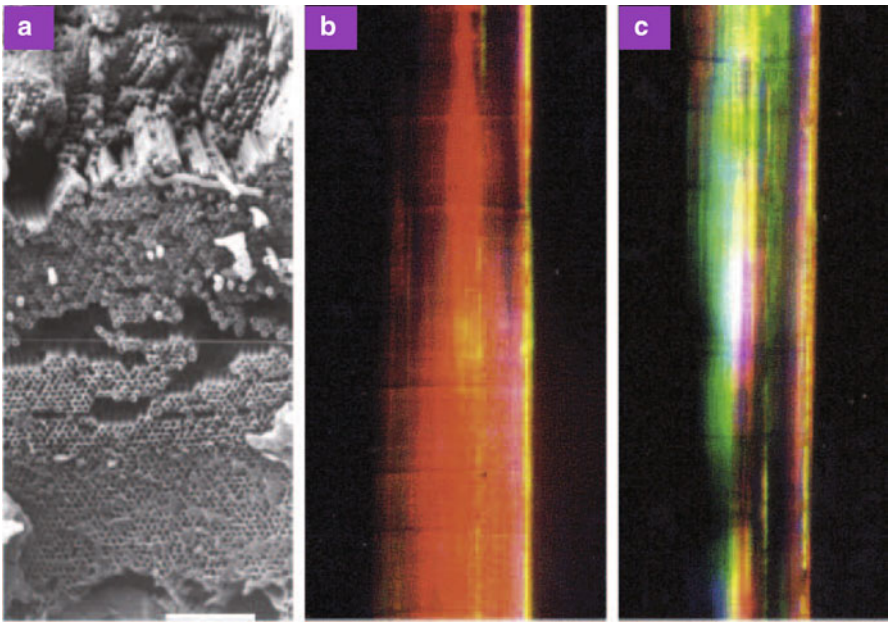

Fig. 8.27 (**a**) Cross-sectional SEM image of the wall region of a spine in the sea mouse *Aphrodita* sp. (**b**) and (**c**) Optical images of a spine showing the color change when the orientation in the horizontal plane varies (by 90°) with respect to the direction of the light source. Scale bar: (**a**) 8 μm (Reproduced from [45])

along this direction. As a result, strong reflection for frequency within this partial bandgap is expected, leading to iridescent structural coloration. Iridescence can be understood by the fact that partial photonic bandgaps are direction dependent.

8.5.4.1 2D Photonic Crystal

The spines of the sea mouse *Aphrodita* sp. (Polychaeta: Aphroditidae) display spectacular iridescence. A spine appears normally dull red in color. However, if illuminated perpendicularly to its axis, different colors can be seen as stripes running parallel to the axis, as shown in Fig. 8.27. SEM characterizations revealed that the spines consist of a wall and a hollow center [120]. The wall region is composed of hollow cylinders, made of pure α-chitin, along the spine axis. The hollow cylinders are close-packed hexagonally, forming a 2D photonic-crystal structure. The cylinders have thicker walls near the spine edge, but after a few layers the wall thickness slightly decreases to a constant value. The spacing of adjacent layers of cylinders is about 0.51 μm and remains constant throughout the wall cross-section. From the calculated photonic band structure of the 2D photonic crystal, there exists a partial photonic bandgap along the $\Gamma - M$ direction, responsible for the observed structural coloration and iridescence.

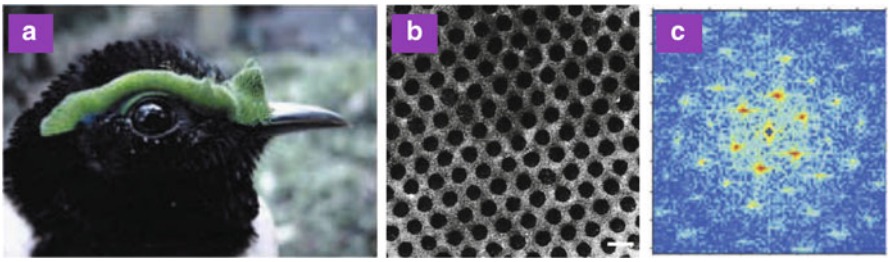

Fig. 8.28 (**a**) Optical image of *P. castanea*. (**b**) TEM image of the nanostructured arrays of the dermal collagen fibers. (**c**) 2D Fourier power spectrum of the TEM image showing discrete bright points of spatial frequency. Scale bar: (**b**) 200 nm (Reproduced from [121])

Structural blue and green colors occur in the skin of a broad diversity of birds from many avian orders and families. Structural characterizations with electron microscopy revealed that the dermal collagen layer contains quasi-ordered or ordered arrays of parallel collagen fibers [121], which are responsible for the skin coloration. The arrays of collagen fibers in the skin of most birds are quasi-ordered, but in *Philepitta castanea* (Eurylaimidae) the collagen fibers are exceptionally ordered, arranged in a hexagonal array, as shown in Fig. 8.28. This ordered arrangement of the collagen fibers manifests a 2D hexagonal photonic crystal, confirmed by a hexagonal pattern of spatial frequency peaks in the power spectrum, obtained from a 2D Fourier analysis.

The most remarkable example of 2D photonic crystals in the biological world resides in peacock feathers [122–125]. Over the centuries, humanity has been impressed by the splendor of the colors of peacocks. The coloration of peacock feathers had puzzled scientists for a long time. More than 300 years ago, Hook and Newton studied peacock feathers by optical observations and suggested that their colors were produced by thin films. The ultimate physical mechanism of the color production was, however, uncovered only recently [124, 125].

The male peacock tail contains spectacular beauty because of the brilliant, iridescent, diversified colors, and the intricate, colorful eye patterns. In the eye pattern of a tail feather of a male green peacock (*Pavo muticus*), blue, green, yellow, and brown feathers can be found, as shown in Fig. 8.29. A typical peacock tail feather possesses a central stem with an array of barbs on each side. Barbs are colorless. On each side of a barb there is an array of flat barbules. Perceived feather colors are from barbules. Each barbule has connected round indentations of typically about 20–30 μm. The round indentations have a smoothly curved crescent-like profile in transverse cross-section. From transverse cross-sectional SEM images, a barbule consists of a medullary core of about 3 μm enclosed by a cortex layer. The medulla consists of randomly dispersed keratin and melanin. In contrast, the cortex layer displays a regular structure. The outer surface of the cortex is a thin layer of keratin. Beneath the surface keratin layer, there is a 2D photonic-crystal structure, made up of an array of melanin rods connected by keratin. The remaining hollows

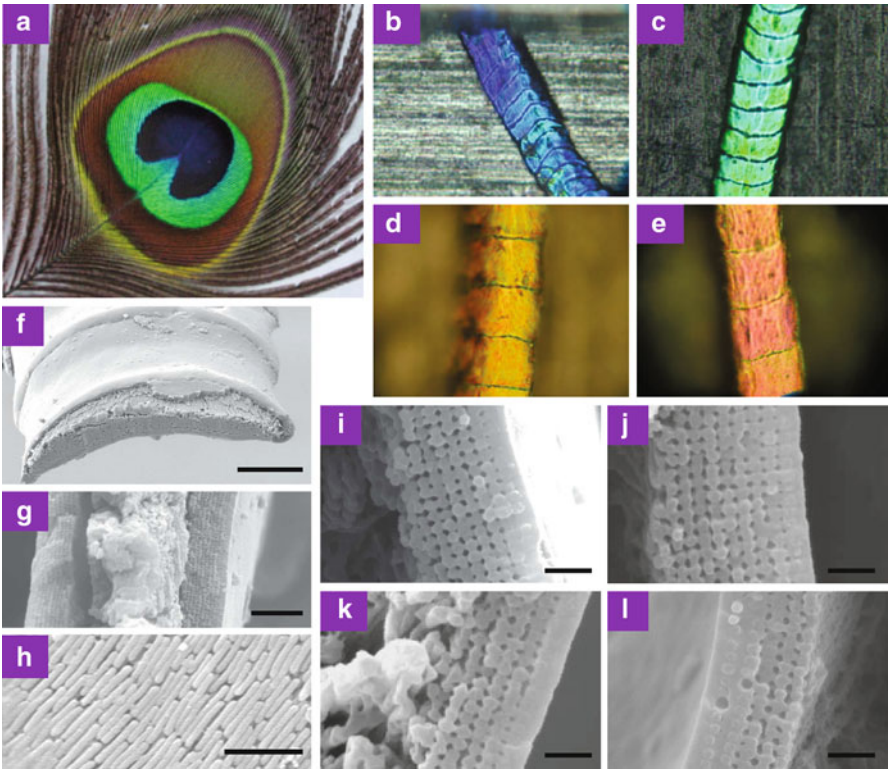

Fig. 8.29 (**a**) Eye pattern of a tail feather of a male green peacock *P. muticus*. (**b**)–(**e**) Optical microscopic images of *blue* (**b**), *green* (**c**), *yellow* (**d**), and *brown* (**e**) barbules. (**f**)–(**l**) SEM images of barbules. (**f**) Perspective view of a sectioned yellow barbule. (**g**) Transverse cross-section of a green barbule. (**h**) Longitudinal cross-section of a green barbule with the surface keratin layer removed. Melanin rods can be clearly seen. (**i**)–(**l**) Transverse cross-sectional images of *blue* (**i**), *green* (**j**), *yellow* (**k**), and *brown* (**l**) barbules. Scale bars: (**f**) 10 μm; (**g**) 2 μm; (**h**) 1 μm; and (**i**)–(**l**) 500 nm

are air holes. Melanin rods are parallel to the cortex surface, running along the axis of a barbule. Photonic-crystal structures in all differently colored barbules are quite similar. In the blue, green, and yellow barbules, the lattice structure is a square lattice, whereas in the brown barbule it is a rectangular lattice. The only differences are the lattice constant (rod spacing) and the number of periods (melanin rod layers) along the direction normal to the cortex surface. The lattice constant for the blue, green, and yellow barbules is 140, 150, and 165 nm, respectively. In the brown barbule, the lattice constant is 150 and 185 nm along the directions parallel and perpendicular to the cortex surface, respectively. The number of periods is 9–12 for the blue and green barbules, and about 6 for the yellow barbules. The brown barbules have the least number of periods, about 4. These differences in the lattice constant and number of periods in differently colored barbules can give rise to diversified coloration.

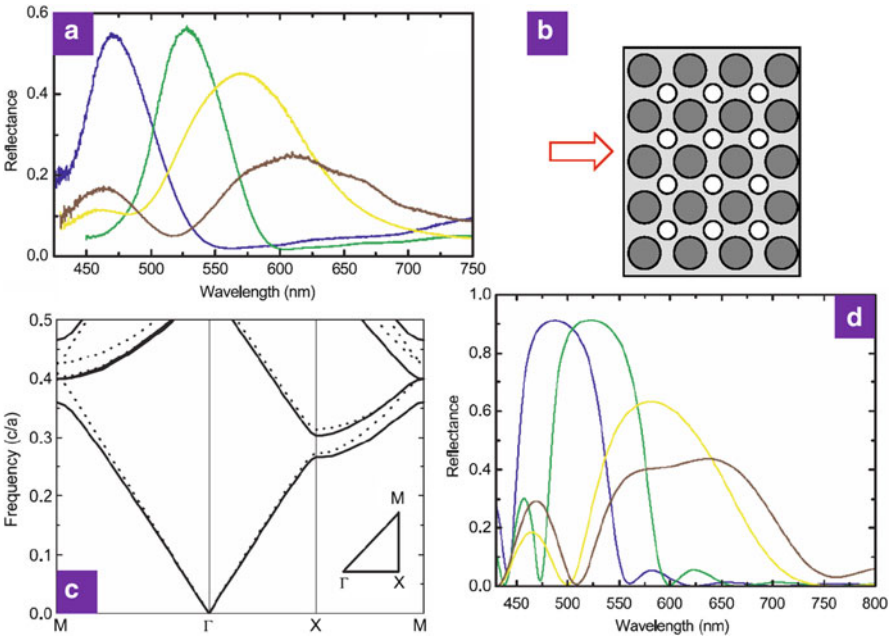

Fig. 8.30 (**a**) Measured reflection spectra of differently colored barbules of the male *P. muticus* under normal incidence. *Blue, green, yellow, and brown lines* represent the results for blue, green, yellow, and brown barbules, respectively. (**b**) Schematic of a 2D photonic crystal used in simulations. *Light gray area, dark gray dot, and white dot* indicate keratin matrix, melanin rod, and air hole, respectively. The *red arrow* indicates the direction perpendicular to the cortex surface. (**c**) Calculated photonic band structure for the electric vector parallel (*solid lines*) and perpendicular (*dashed lines*) to the melanin rods. Frequency is in units of c/a, where c is the light speed in vacuum and a is the lattice constant. The *inset* shows the irreducible Brillouin zone with Γ, X, and M representing its center, edge center, and corner, respectively. Note that the $\Gamma - X$ direction is along the direction normal to the cortex surface. (**d**) Calculated reflection spectra under normal incidence for generic 2D photonic crystals with a finite number of periods. *Blue, green, yellow, and brown lines* represent the results for blue, green, yellow, and brown barbules, respectively, and the corresponding number of periods is 10, 10, 6, and 4, respectively (Reproduced from [124])

Measured reflection spectra for differently colored barbules with a microspectrophotometer under normal incidence are shown in Fig. 8.30. The blue and green barbules display a single reflection peak, while the yellow and brown barbules show two reflection peaks. For the blue and green barbules, their reflection peaks are located into blue and green wavelengths, respectively. For the yellow barbule, the main peak ranges from green to orange wavelengths, indicating that the yellow color is a mixed color. The intensity of the secondary peak at blue wavelengths is too small to contribute to coloration. For the brown barbule, however, the peak at blue wavelengths has a intensity comparable to the broad reflection peak ranging from green, yellow, orange to red wavelengths.

To explore the origin of coloration in the feather barbules, the photonic band structure of an infinite 2D photonic crystal was calculated by a PWE method, shown in Fig. 8.30c. The structural parameters for this photonic crystal were taken from the measurements, i.e., $r_{\text{rod}}/a = 0.4$ and $r_{\text{air}}/a = 0.25$, where r_{rod} and r_{air} are the radii of the melanin rods and air holes, respectively, and a is the lattice constant. The refractive indices of keratin and melanin were taken to be 1.54 and 2.0, respectively. This 2D photonic crystal does not exhibit a complete photonic bandgap. However, a partial photonic bandgap for both polarizations exists along the $\Gamma - X$ direction. It is noted that the photonic band structure for the two polarizations shows a small difference at low frequencies (corresponding to the visible wavelengths), and it differs at high frequencies (corresponding to the UV wavelengths or below). The difference between the midgap frequencies for the two polarizations is rather small. This indicates that the peacock feather barbules exhibit small polarization effects in coloration. Strong reflections are expected for frequencies within the partial photonic bandgap along the $\Gamma - X$ direction, responsible for barbule coloration. It should be mentioned that the partial photonic bandgap shifts to a higher frequency range with the increasing angle of incidence, leading to iridescence.

For blue, green, and yellow barbules, their colors stem from the partial photonic bandgap of the 2D photonic crystal in the cortex. This can be confirmed by the calculated reflection spectra of generic 2D photonic crystals with a finite number of periods by a TMM, shown in Fig. 8.30d. The calculated reflection spectra correctly reproduce the main features of the experiments.

Note that brown is a mixed color. The partial photonic bandgap can only cause a reflection peak covering green, yellow, orange to red wavelengths. Simulations [124, 125] revealed that the Fabry–Perot interference plays an important role in the color production of brown barbules. For any finite photonic crystal, Fabry–Perot interference should exist owing to the interference from their two surfaces, leading to oscillating side peaks on the two sides of the reflection peak produced by the partial photonic bandgap. For a finite photonic crystal with a large number of periods, the reflection peak produced by the partial photonic bandgap is dominant, while the contribution of the side peaks to coloration by Fabry–Perot interference is negligible. However, with the decreasing number of periods, side peaks also play a role in coloration, giving rise to an additional color. For brown barbules, the number of periods is the least. As a result, the Fabry–Perot interference leads to an additional blue reflection peak which is comparable to the main peak from the partial photonic bandgap, eventually giving rise to a structural brown color by color mixing. It was found [125] that other factors such as the interdistance and missing air holes between the two melanin layers nearest to the cortex surface are important in the production of the structural brown color.

Peacock feathers take advantage of a 2D photonic crystal in the barbule cortex for coloration. The strategies for diversified color production are very ingenious and rather simple, i.e., by means of the variation of the lattice constant and the number of periods. Varying the lattice constant will shift the midgap frequency of the partial photonic bandgap, leading to different colors. The reduction in the number of periods may cause an additional color, resulting in mixed coloration. By the two strategies, diversified structural colors can be produced.

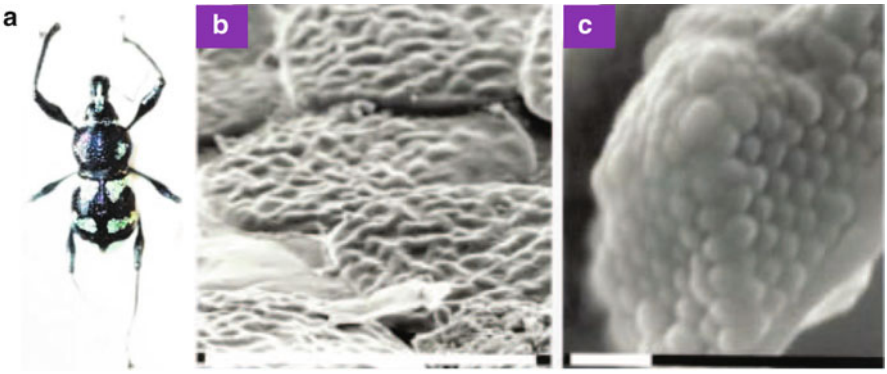

Fig. 8.31 (**a**) Photograph of the weevil *P. argus*. (**b**) SEM image showing several partially overlapping scales. (**c**) Cross-sectional SEM image of a region of a scale. Scale bars: (**b**) 100 μm and (**c**) 1 μm (Reproduced from [126])

8.5.4.2 3D Photonic Crystal

In addition to 2D photonic crystals, 3D photonic crystals that are periodic in three dimensions are also present in the biological world. Revealed 3D photonic crystals display various forms exhibiting different optical effects. Unlike 1D and 2D photonic structures, the determination of the detailed structural configurations for 3D photonic structures is rather difficult and challenging, especially for those with complicated connectivity and topology. This is because commonly used electron microscopy such as SEM and TEM can only offer 2D structural information for certain sectioned orientations. Electron tomography could be very helpful in the reconstructions of 3D photonic structures. The correct determination of complex 3D photonic structures are, however, still a difficult task even with electron tomography. As a result, one has to be very careful in the recognition and reconstruction when based on a few 2D SEM or TEM sectioned images.

The first 3D photonic crystal revealed in the biological world might be the one in the scales of the weevil *Pachyrhynchus argus* [126], as shown in Fig. 8.31. The weevil displays a metallic color coming from the scales, about 0.1 mm in diameter, occurring in the patches on the top and sides of its body. The scales are flat, lying parallel to the body. The colored scales show a yellow-green color in reflected light and a complementary purple color in transmitted light from most directions. These colored scales consist of an outer shell and an inner part. The inner part is an array of transparent spheres, each with a diameter of 250 nm, arranged in the close-packing order. This arrangement is similar to that in opal, i.e., spheres that are arranged in a face-centered cubic lattice. The invariant yellow-green color perceived is a result of global averaging of different domains since the scales contain differently oriented domains of opal-like structures. Moreover, iridescence is absent due to the averaging effects, leading to nearly the same bright coloration from every direction. This could be useful for interspecific color or pattern recognition.

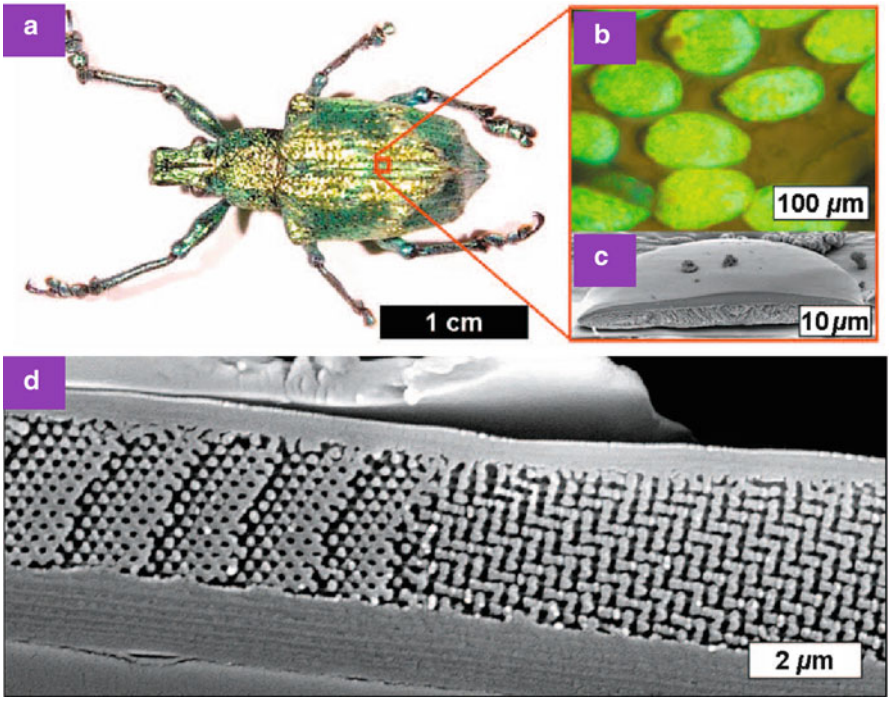

Fig. 8.32 (**a**) Optical image of the weevil *L. augustus*. (**b**) Optical microscopic image of individual scales attached to the exoskeleton. (**c**) Cross-sectional SEM image of a scale. (**d**) Close-up cross-sectional SEM image of a region of a scale (Reproduced from [128])

Among various 3D photonic structures, photonic crystals with a diamond lattice are the "champion" structures because they may create the largest complete photonic bandgaps [127], but the artificial fabrication of such photonic structures at the visible regime is still very challenging. This diamond-based photonic crystal was, however, found in the weevil *Lamprocyphus augustus* [128], as shown in Fig. 8.32. The weevil shows bright green coloration that is nearly angle-independent. The green coloration derives from leaf-like cuticle scales attached to the weevil's exoskeleton. By combining a high-resolution structure analysis technique based on sequential focused ion beam milling and SEM imaging, a 3D photonic-crystal structure with a diamond-based lattice was revealed in the scale interior. The measured average lattice constant is about 450 nm. Within individual scales, the diamond-based photonic-crystal structures are assembled in the form of differently oriented single-crystalline micrometer-sized domains with only selected lattice planes facing the top surface of the scales. Simulations revealed that partial photonic bandgaps exist along different directions with different midgap frequencies, yielding different coloration. The nearly angle-independent green coloration in the scales is thus a combination of all contributions from the differently oriented diamond-based photonic-crystal structures.

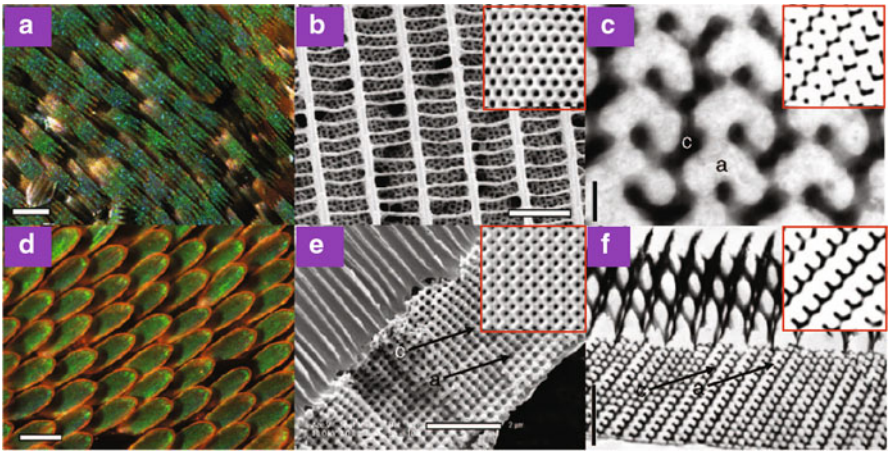

Fig. 8.33 Nanostructures for structural coloration in the scales of lycaenid and papilionid butterflies. (**a**) Optical microscopic image of the ventral wing cover scales of *C. gryneus*. (**b**) SEM image of the dorsal surface of a *C. gryneus* scale showing disjoint crystallites beneath windows created by a network of parallel, longitudinal ridges and slender, spaced cross-ribs. The inset shows the simulated SEM (111) projection from a thick slab of a level set single gyroid nanostructure. (**c**) TEM image of the *C. gryneus* nanostructure showing a distinctive motif, uniquely characteristic of the (310) plane of the gyroid morphology. The inset shows a matching simulated (310) TEM section of a level set single gyroid model. (**d**) Optical microscopic image of the dorsal wing cover scales of *P. sesostris*. (**e**) SEM image of the lateral surface of the wing scale nanostructure of *P. sesostris* showing fused polycrystalline domains beneath columnar windows created by a network of ridges and spaced cross-ribs. The fractured face features a square lattice of air holes in chitin. The inset shows the simulated SEM (100) projection from a thick slab of a level set single gyroid nanostructure. (**f**) TEM image of the *P. sesostris* nanostructure showing a distinctive motif, uniquely characteristic of the (211) plane of the gyroid morphology. The inset shows a matching simulated (211) TEM section of a level set single gyroid model. The labels *c* and *a* in (**c**), (**e**), and (**f**) indicate chitin and air void, respectively. Scale bars: (**a**) and (**d**) 100 μm; (**b**) 2.5 μm; (**c**) 200 nm; and (**e**) and (**f**) 2 μm (Reproduced from [137])

In additional to multilayers, 3D photonic crystals are also exploited in butterflies for structural coloration, e.g., in papilionid and lycaenid butterfly scales [129–137]. Revealed 3D photonic structures exhibit various forms and complexity, attributed to simple cubic [129] and face-centered cubic [130] structures, and gyroid structures [135–137].

The wings of the butterflies *Callophrys gryneus* (Lycaenidae) and *Parides sesostris* (Papilionidae) display vivid structural colors. Structural characterizations based on electron microscopy and small angle X-ray scattering [137] show that these wing colors are caused by a gyroid (I_4132) photonic crystal in the scales, a bicontinuous triply periodic structure of the network of chitin and air, as shown in Fig. 8.33. The measured lattice parameter is about 306 nm for *C. gryneus* and about 288 nm for *P. sesostris*. The estimated filling fraction is about 0.34 and 0.3 for *C. gryneus* and *P. sesostris*, respectively. Photonic band structure calculations revealed

that there exist three relatively closely spaced partial photonic bandgaps along the (110), (111), and (200) directions for the butterfly gyroid photonic crystal, which are the origin of the structural coloration of the wings.

8.5.5 Amorphous Photonic Structure

According to their arrangements, photonic structures can be classified into three classes: ordered structures with both short- and long-range order, quasi-ordered or amorphous structures with only short-range order, and random structures with neither short- nor long-range order. These three classes of photonic structures have different optical response, leading to structural coloration with distinctive features. For ordered photonic structures, they can produce iridescent structural coloration. The iridescence of ordered photonic structures stems from long-range order. On the other hand, quasi-ordered or amorphous photonic structures can cause angle-independent structural coloration, i.e., non-iridescent structural coloration. Random photonic structures that lack both short- and long-range order may only produce white colors.[6]

In addition to ordered categories in the biological world, there also exist quasi-ordered or amorphous photonic structures that possess only short-range order, giving rise to non-iridescent structural coloration. The most known example is the spongy structure of keratin in the feather barbs of many birds. These non-iridescent colors were hypothesized over 100 years ago to be produced by incoherent scattering from individual scatters, namely, individual air vacuoles [1, 17, 138, 139], where phase relations among scattered light are random. Two types of incoherent scattering mechanisms were proposed: one is Rayleigh scattering [138] and the other is Tyndall or Mie scattering [1, 17, 139].

In 1934 Raman opposed this incoherent-scattering hypothesis with the thorough observations of the feathers of the bird *Coracias Indica* which displays a non-iridescent blue color under natural light [140]. He concluded that incoherent scattering such as a Tyndall effect was definitely insufficient to explain the observations, and suggested that the diffraction by the air cavities and the interference from the surfaces of minute films were responsible for the non-iridescent blue feather barb coloration.

In 1970s Dyck challenged the Rayleigh model for the blue coloration of feather barbs [141, 142]. He noticed that the reflection spectra of many bird feathers display discrete peaks, which is inconsistent with the prediction of a continued scattering efficiency that is inversely proportional to the fourth power of wavelength by the Rayleigh law. Dyck hypothesized that coherent light scattering by the ordered matrix of air vacuoles and keratin was the cause of the blue coloration.

[6] White colors are always of structural origins.

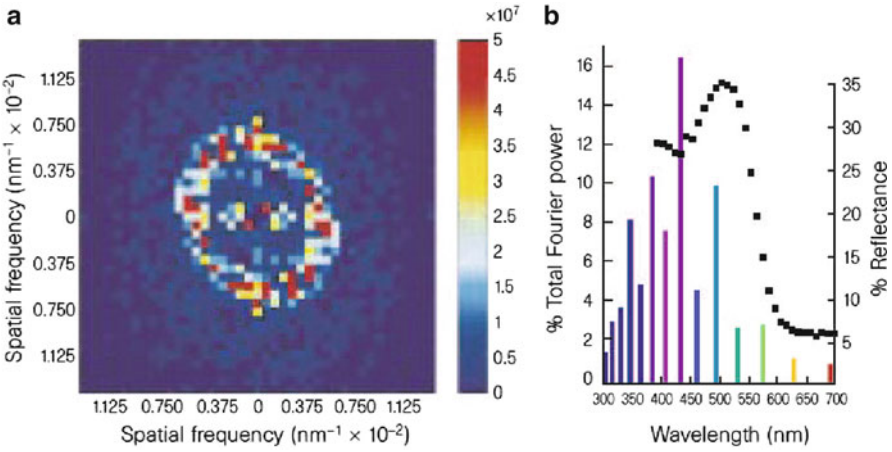

Fig. 8.34 (**a**) 2D Fourier power spectrum of the spongy keratin matrix in a blue feather barb of *Cotinga maynana*. (**b**) Observed reflection spectrum of a blue feather barb (*black squares*, right axis) and predicted reflection spectrum (*bars*, left axis) based on the 2D Fourier power spectrum in (**a**) (Reproduced from [143])

In late 1990s Prum and coworkers demonstrated ambiguously by structural analyses in the reciprocal space that the blue coloration of feather barbs is indeed produced by coherent light scattering [143, 144]. They performed 2D Fourier analyses for cross-sectional TEM images of the spongy keratin layer in the blue feather barbs of some birds, and revealed a nearly circular ring around the origin in 2D Fourier power spectra, as shown in Fig. 8.34. The existence of a ring in 2D Fourier power spectra indicates that the spongy keratin has only short-range order, which will lead to coherent light scattering and hence cause the non-iridescent blue coloration. Recently, they employed small-angel X-ray scattering to characterize the nanostructures of the blue feather barbs of some birds [145, 146], as shown in Fig. 8.35. Clearly, the scattering spectra exhibit rings, implying again that these nanostructures possess only short-range order, resulting in non-iridescent coloration via coherent light scattering.

To compare with measurements quantitatively, a simply theory has been frequently used [6, 143–146], namely, simply translating 2D Fourier power spectra or small-angle X-ray scattering spectra into reflection spectra by imposing a Bragg-like condition

$$\frac{2\pi}{\lambda}\tilde{n} = \frac{k_{\max}}{2}, \tag{8.9}$$

where $\tilde{n}$ is the averaged refractive index of a nanostructure and $k_{\max}$ is the peak value of the spatial frequencies. It should be mentioned that this simply theory is valid only for very weak scattering. The application to amorphous photonic structures seems problematic.

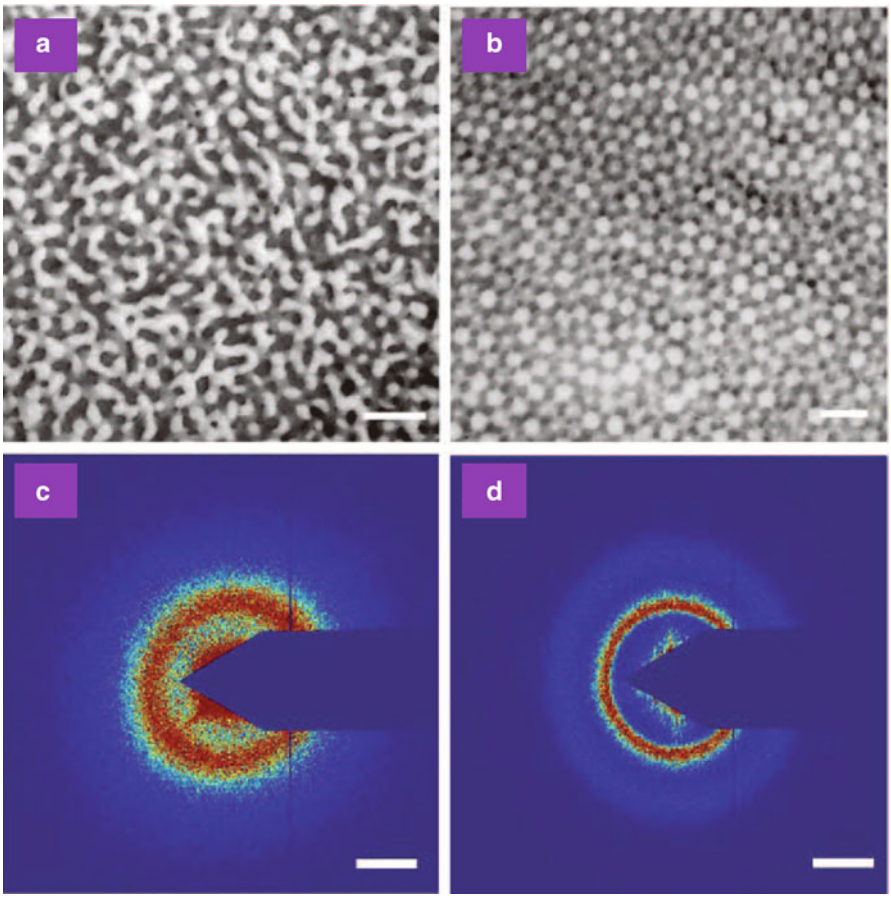

Fig. 8.35 (**a**) and (**b**) Cross-sectional TEM images of the nanostructures from back contour feather barbs of *Sialia sialis* and *C. maynana*, respectively. (**c**) and (**d**) Small-angle X-ray scattering data for feather barbs of *S. sialis* and *C. maynana*, respectively. Scale bars: (**a**) and (**b**) 500 nm; and (**c**) and (**d**) 0.025 nm^{-1} of spatial frequency (Reproduced from [145])

Coherent light scattering is conceptually the correct understanding for the non-iridescent structural coloration produced by amorphous photonic structures [6, 141–147], but it is not the ultimate physical mechanism. Moreover, the simple translation of Fourier power spectra into reflection spectra by using the Bragg-like condition could be problematic since the Bragg condition is only valid for very weak scattering or dilute scatters. This is because for amorphous photonic structures light scattering is far from weak owing to the short-range order. On the other side, the translation procedure relies solely on the structural information, i.e., the structure factor. As is known, reflection is related not only to the structure factor but also to the detailed spatial distribution of refractive index.

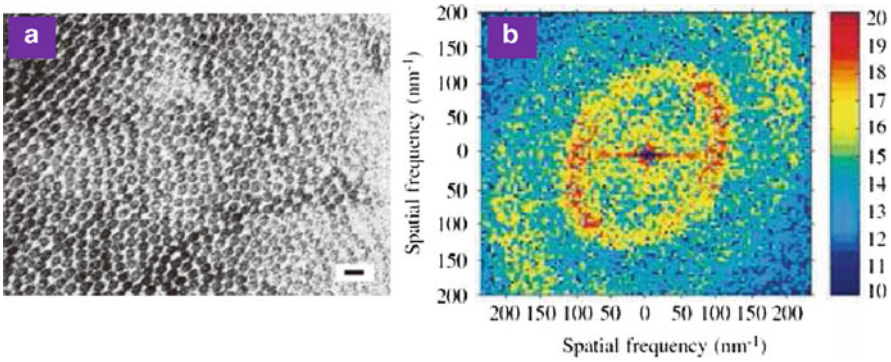

Fig. 8.36 (**a**) TEM image of a collagen array from dark blue caruncle tissue of *Neodrepanis hypoxantha*. (**b**) 2D Fourier power spectrum of the tissue. Scale bar: (**a**) 200 nm (Reproduced from [150])

Recently, the optical response of amorphous photonic structures was studied numerically by the authors with rigorous methods to solve Maxwell's equations [148, 149]. From the calculated photon density of states (PDOS) for amorphous photonic structures, there exist angle-independent (isotropic) *photonic pseudogaps* due to coherent light scattering from short-range order. Unlike photonic bandgaps in photonic crystals within which the PDOS is zero, photonic pseudogaps show nonzero dips in the PDOS. Our results indicate unambiguously that photonic pseudogaps are the ultimate physical origin for the non-iridescent structural coloration of amorphous photonic structures. Non-iridescence can be understood by the fact that light is scattered evenly in all directions since there is no preferred orientation in amorphous photonic structures due to the lack of long-orange order.

In feather barbs, the amorphous photonic structures responsible for the blue coloration are mostly a keratin network in the spongy medullary layer [143–147], with keratin bars and air channels in tortuous and twisting forms, as shown in Fig. 8.35a. These nanostructures possess only short-range order and are responsible for the iridescent structural coloration. Another kind of nanostructure was found in the blue back plumage of the Eastern Bluebird (*S. sialis*) where the air cavities are nearly spherical and close-packed [146], as shown in Fig. 8.35b. The nanostructure of spherical air cavities also exhibits short-range order.

Amorphous photonic structures were also found in the structurally colored skin of some birds [121, 150]. The dermis of structurally colored skin consists of a thick (100–500 μm) layer of collagen. TEM characterizations revealed that most of the color producing dermal collagen layers consist of a quasi-ordered array of parallel collagen fibers as shown in Fig. 8.36. 2D Fourier analyses showed that the array of collagen fibers has short-range order, indicating that the collagen fibers are arranged in the form of 2D amorphous photonic structures. The dermal colors are determined by the nanostructure of the collagen arrays via coherent light scattering.

In addition to birds, amorphous photonic structures are also present in beetles [148, 149, 151, 152]. For example, the scales of the longhorn beetle *Anoplophora graafi* contain a random-close-packing photonic structure of chitin nanoparticles [148], while the scales of the longhorn beetle *Sphingnotus mirabilis* possess a disordered bi-continuous photonic structure of chitin [149]. Both photonic structures have only short-range order and are responsible for the non-iridescent structural coloration of the scales.

As shown in Fig. 8.37, the beetle *A. graafi* has a dull metallic blue or green color on its elytra marked with brilliant greenish white lateral stripes. Under optical microscopy, these stripes are composed of differently colored scales which are seed-like, about 50 μm long and 20 μm wide. Each scale has a distinct non-iridescent color and the scale color can cover almost the whole visible range. The perceived greenish white is thus a mixed color resulting from differently colored scales in a pointillistic way. Cross-sectional SEM images revealed that the interior of scales is an array of chitin nanoparticles in a form of random close-packing (RCP), confirmed by comparing with the generated RCP structure. The 2D radial distribution function indicates that the RCP photonic structure in the scale interior possesses only short-range order.

To get insight into the coloration mechanism of RCP photonic structures, the PDOS of model RCP photonic structures were calculated, as shown in Fig. 8.38. Two prominent dips (photonic pseudogaps) appear in the calculated PDOS. Compared with the PDOS, the calculated reflection peaks and photonic pseudogaps show a one-to-one correspondence. This indicates that photonic pseudogaps are the ultimate cause of the non-iridescent structural coloration of RCP photonic structures.

8.6 Outlook

Photonic structures occurring in the biological world show striking diversity, complexity, and delicacy. They have received increasing research interest from a variety of fields ranging from physics, biology, and chemistry to material science due to their fundamental and application-oriented significance. The studies of natural photonic structures and resultant structural colors may not only provide insights into our understanding of their biological and physical aspects but also offer valuable inspirations. Despite considerable advances made especially in recent years, there exist still many important questions and challenging problems to be answered. Interesting topics related to photonic structures in the biological world include their evolution, structural formation, function, structural characterization, material determination, mechanism, and bio-inspired design and fabrication.

The evolution of natural photonic structures, a fundamental problem, is poorly researched. Although some progress has been made in recent years, there remain a number of interesting and challenging problems [2, 58, 59, 145, 153–156] such as the evolution mechanism, how natural photonic structures develop and form during individual growth, and the underling genetic mechanisms that determine phenotype.

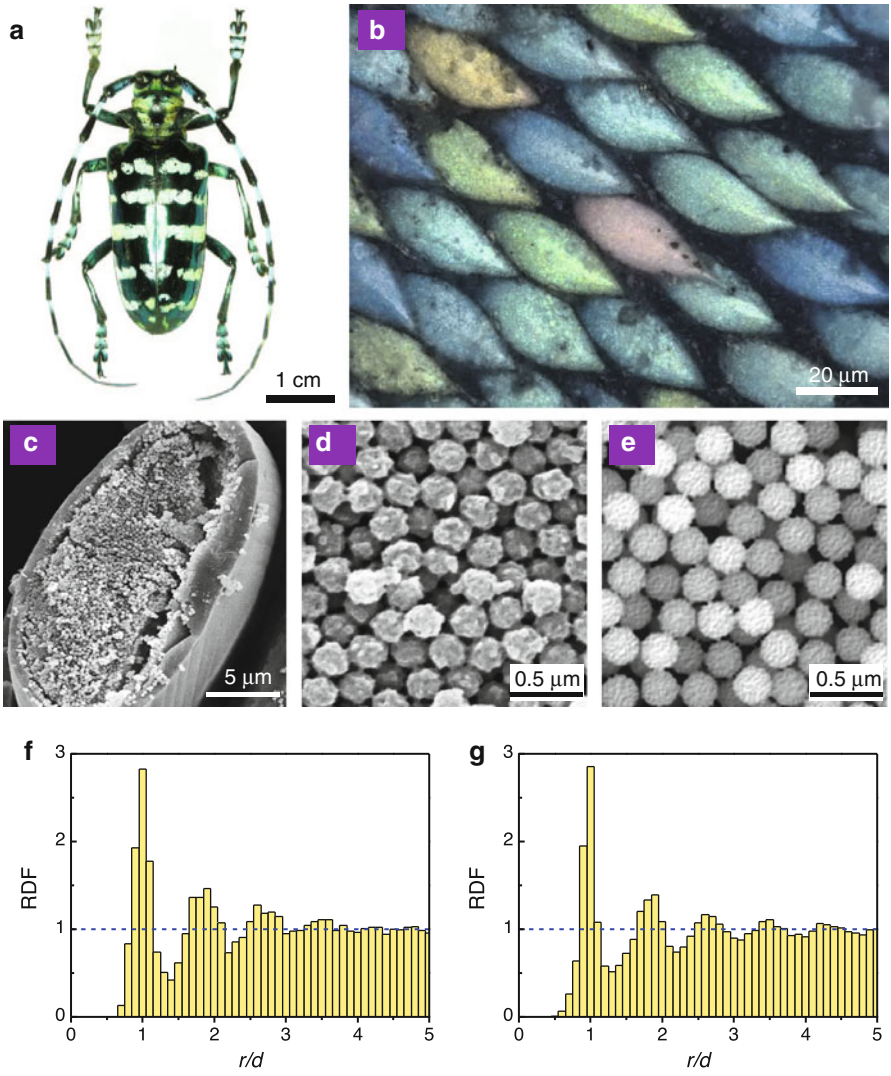

Fig. 8.37 (**a**) Optical image of *A. graafi*. (**b**) Optical microscopic image of a greenish white stripe under 500× magnification. (**c**) Cross-sectional SEM image of a green scale. (**d**) Close-up cross-sectional SEM image of the interior of a green scale. (**e**) Cross-section of a generated RCP structure of equal spheres with surfaces roughened arbitrarily. (**f**) and (**g**) Histogram of the 2D radial distribution function with (**f**) for the RCP structure in the green scale and (**g**) for the generated one, where d is the diameter of nanoparticles (Reproduced from [148])

The functions of natural photonic structures are closely related to their evolution. Structural coloration in animals often serves primarily as intraspecific communication such as species recognition, mate choice, and intrasexual competition, and also as interspecific interactions such as predator avoidance by using aposematic

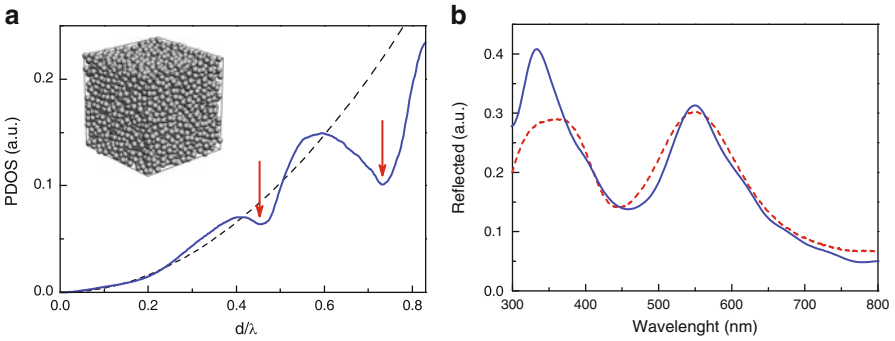

Fig. 8.38 (**a**) Calculated PDOS of a model RCP photonic structure (*inset*) as a function of reduced frequency d/λ, where d is the diameter of the nanoparticles and λ is the wavelength in vacuum. The PDOS of a homogeneous medium with a refractive index of 1.38 (*dashed red line*) is given for comparison. Photonic pseudogaps are indicated by *arrows*. (**b**) Calculated (*solid line*) and measured (*dashed line*) reflection spectra. Measured reflection spectrum for green scales was obtained by macro-optical spectroscopy. In the calculations, the nanospheres take a refractive index of 1.56, a typical value for chitin, and their diameter is assumed to be 240 nm, a typical value for the chitin nanoparticles in green scales (Reproduced from [148])

and cryptic coloration [157]. Noncommunicative functions of natural photonic structures have also been proposed such as thermoregulation [158], structural support and strengthening [159, 160], friction reduction [161], and photoprotection and visual enhancement [162]. Most of the biological, physical, and physiological functions are hypothetical, and more research efforts are hence needed.

Structural determinations are essential in understanding structural coloration. For simple natural photonic structures such as thin films, multilayers, and 2D photonic crystals, they can be explored by SEM and TEM. As aforementioned, however, structural determinations are sometimes extremely difficult especially for natural photonic structures with complex building units or connectivity, e.g., nontrivial 3D photonic structures, since frequently used tools such as SEM and TEM can only offer 2D structural information in certain orientations. Combinational, correlational, and advanced tools are highly desired in order to get correct structures.

Another important and also less known and researched problem is about the constituent materials and their distribution in natural photonic structures, particularly with refractive index (both real and imaginary components) and dispersion across the relevant wavelength range. Additionally, surrounding materials are sometimes also important in determining the optical response of natural photonic structures. The structural and optical properties of surrounding materials ought to be studied in detail.

Among the relatively better understood aspects of natural photonic structures are the mechanisms of their structural color production. Generally, structural coloration can be understood in terms of interference, diffraction, and scattering. As is shown, natural photonic structures exhibit astonishing diversity and complexity. For complicated photonic structures with architectures of different levels, their color

production may be the interplay among interference, diffraction, and scattering, which could obstacle considerably the finding of ultimate physical mechanisms. Moreover, the combination of these optical effects may even lead to new optical phenomena. For example, complicated photonic band structures occurring in photonic crystals are due to the combination of these optical effects. The ultimate physical cause of iridescent structural coloration in photonic crystals is direction-dependent partial photonic band gaps [124, 126, 128, 137]. In amorphous photonic crystals, on the other side, isotropic photonic pseudogaps are the ultimate physical cause of non-iridescent structural coloration [148, 149].

Nature usually takes the strategy of maximal achievement at minimal cost. As a result of evolution, photonic structures exploited in the biological world may be optimal in the sense of their biological, physical, or even physiological functions. Natural photonic structures in step with their coloration strategies are a valuable source of inspiration. In recent years, there has been a growing interest in biomimetic and bio-inspired design [163–166]. The use of structural color is environmentally promising since it bypasses the need for chemical pigments, which are often toxic. Bio-inspired photonic structures and structural colors may have potential applications in a variety of industries such as photonics, display, painting, and textile. Natural photonic structures and the ingenious ways of light steering may have been a great source of inspiration in our design and fabrication of new optical materials and devices for future technological applications.

References

1. Fox, D.L.: Animal Biochromes and Structural Colours. University of California Press, Berkeley (1976)
2. Ghiradella, H.: Appl. Opt. **30**, 3492 (1991)
3. Srinivasarao, M.: Chem. Rev. **99**, 1935 (1999)
4. Parker, A.R.: J. Opt. A Pure Appl. Opt. **2**, R15 (2000)
5. Vukusic, P., Sambles, J.R.: Nature (London) **424**, 852 (2003)
6. Prum, R.O.: In: Hill, G.E., McGraw, K.J. (eds.) Bird Coloration, vol. 1, p. 295. Harvard University Press, Cambridge, MA (2006)
7. Berthier, S.: Iridescences: The Physical Colors of Insects. Springer, New York (2007)
8. Kinoshita, S., Yoshioka, S., Miyazaki, J.: Rep. Prog. Phys. **71**, 076401 (2008)
9. Vigneron, J.P., Simonis, P.: Adv. Insect Physiol. **38**, 181 (2010)
10. Michelson, A.A.: Phil. Mag. **21**, 554 (1911)
11. Walter, B.: Die Oberflöchen- orde Schillerfarben. Vieweg, Braunschweig (1895)
12. Rayleigh, L.: Phil. Mag. **37**, 98 (1919)
13. Biedermann, W.: Festschrift Zum Siebzigsten Geburtstage von Haeckel, p. 215. Denschriften Med. Naturwiss. Ges., Jena (1904)
14. Mallock, A.: Proc. R. Soc. Lond. A **85**, 598 (1911)
15. Merritt, E.: J. Opt. Soc. Am. Rev. Sci. Instrum. **11** 93 (1925)
16. Onslow, H.: Phil. Trans. **211**, 1 (1923)
17. Mason, C.W.: J. Phys. Chem. **27**, 201 (1923)
18. Mason, C.W.: J. Phys. Chem. **27**, 401 (1923)
19. Mason, C.W.: J. Phys. Chem. **30**, 383 (1926)

20. Mason, C.W.: J. Phys. Chem. **31**, 321 (1927)
21. Mason, C.W.: J. Phys. Chem. **31**, 1856 (1927)
22. Frank, F., Ruska, H.: Naturwiss **27**, 229 (1939)
23. Born, M., Wolf, E.: Principles of Optics. Cambridge University Press, Cambridge (1999)
24. Rayleigh, L.: Philos. Mag. **41**, 107, 274 (1871)
25. Tyndall, J.: Philos. Mag. **37**, 384 (1869)
26. van de Hulst, H.C.: Light Scattering by Small Particles. Dover, New York (1981)
27. Yablonovitch, E.: Phys. Rev. Lett. **58**, 2059 (1987)
28. John, S.: Phys. Rev. Lett. **58**, 2486 (1987)
29. Joannopoulos, J.D., Johnson, S.G., Winn, J.N., Meade, R.D.: Photonic Crystals: Molding The Flow of Light, 2nd edn. Princeton University Press, Princeton (2008)
30. CVRL Color & Vision database, http://www.cvrl.org/
31. Yeh, P.: Optical Waves in Periodic Media. Wiley, New York (1988)
32. Pendry, J.B., Mackinnon, A.: Phys. Rev. Lett. **69**, 2772 (1992)
33. Bell, P.M., Pendry, J.B., Moreno, L.M., Ward, A.J.: Comput. Phys. Commun. **85**, 306 (1995)
34. Yee, K.S.: IEEE Trans. Antennas Propag. **14**, 302 (1966)
35. Taflove, A., Hagness, S.C.: Computational Electrodynamics: The Finite-Difference Time-Domain Method. Artech House, Norwood, MA (2000)
36. Stefanou, N., Yannopapas, V., Modinos, A.: Comput. Phys. Commun. **132**, 189 (2000)
37. Fox, H.M., Vevers, G.: The Nature of Animal Colours. Sidgwick and Jackson, London (1960)
38. Shevtsova, E., Hansson, C., Janzen, D.H., Kjærandsen, J.L Proc. Natl. Acad. Sci. USA **108**, 668 (2011)
39. Dyck, J.: Biol. Skr. (Copenhagen) **30**, 2 (1987)
40. McGraw, K.J.: Naturwissenschaften **91**, 125 (2004)
41. Yin, H., Shi, L., Sha, J., Li, Y., Qin, Y., Dong, B., Meyer, S., Liu, X., Zhao, L., Zi, J.: Phys. Rev. E **74**, 051916 (2006)
42. Yoshioka, S., Nakamura, E., Kinoshita, S.: J. Phys. Soc. Jpn. **76**, 013801 (2007)
43. Nakamura, E., Yoshioka, S., Kinoshita, S.: J. Phys. Soc. Jpn. **77**, 124801 (2008)
44. Land, M.F.: Prog. Biophys. Mol. Biol. **24**, 75 (1972)
45. Parker, A.R.: J. Roc. Soc. Interface **2**, 1 (2005)
46. Seago, A.E., Brady, P., Vigneron, J.P., Schultz, T.D.: J. Roc. Soc. Interface **6**, S165 (2009)
47. Durrer, H., Villiger, W.: Int. J. Insect Morphol. Embryol. **1**, 233 (1972)
48. Deparis, O., Vandenbem, C., Rassart, M., Welch, V.L., Vigneron, J.P.: Opt. Express **14**, 3547 (2006)
49. Vigneron, J.P., Rassart, M., Vandenbem, C., Lousse, V., Deparis, O., Biro, L.P., Dedouaire, D., Cornet, A., Defrance, P.: Phys. Rev. E **73**, 041905 (2006)
50. Stavenga, D.G., Wilts, B.D., Leertouwer, H.L., Hariyama, T.: Phil. Trans. R. Soc. B **366**, 709 (2011)
51. Noyes, J.A., Vukusic, P., Hooper, I.R.: Opt. Express **15**, 4351 (2007)
52. Vigneron, J.P., Colomer, J.F., Vigneron, N., Lousse, V.: Phy. Rev. E **72**, 061904 (2005)
53. Liu, F., Dong, B.Q., Liu, X.H., Zheng, Y.M., Zi, J.: Opt. Express **17**, 16183 (2009)
54. Arsenault, A.C., Clark, T.J., Von Freymann, G., Cademartiri, L., Sapienza, R., Bertolotti, J., Vekris, E., Wong, S., Kitaev, V., Manners, I., Wang, R.Z., John, S., Wiersma, D., Ozin, G.A.: Nat. Mater. **5**, 179 (2006)
55. Walish, J.J., Kang, Y., Mickiewicz, R.A., Thomas, E.L.: Adv. Mater. **21**, 1 (2009)
56. Anderson, T., Richards Jr., A.: J. Appl. Phys. **13**, 748 (1942)
57. Gentil, K.: Z. Morph. Ökol. Tiere **38**, 344 (1942)
58. Ghiradella, H.: Ann. Entomol. Soc. Am. **77**, 637 (1984); ibid., **78**, 252 (1984)
59. Ghiradella, H.: Microsc. Res. Tech. **27**, 429 (1994)
60. Vukusic, P., Sambles, J.R., Lawrence, C.R., Wootton, R.J.: Proc. R. Soc. Lond. B **266**, 1403 (1999)
61. Gralak, B., Tayeb, G., Enoch, S.: Opt. Express **9**, 567 (2001)
62. Kinoshita, S., Yoshioka, S., Kawagoe, K.: Proc. R. Soc. Lond. B **269**, 1417 (2002)
63. Yoshioka, S., Kinoshita, S.: Proc. R. Soc. Lond. B **271**, 581 (2004)

64. Yoshioka, S., Kinoshita, S.: Proc. R. Soc. Lond. B **273**, 129 (2006)
65. Berthier, S., Charron, E., Boulenguez, J.: Insect Sci. **13**, 145 (2006)
66. Vukusic, P., Sambles, J.R., Lawrence, C.R., Wootton, R.J.: Nature **410**, 36 (2001)
67. Land, M.F., Horwood, J., Lim, M.L.M., Li, D.Q.: Proc. R. Soc. Lond. B **274**, 1583 (2007)
68. Lim, M.L.M., Land, M.F., Li, D.Q.: Science **315**, 481 (2007)
69. Hébant, C., Lee, D.W.: Am. J. Bot. **71**, 216 (1984)
70. Thomas, K.R., Kolle, M., Whitney, H.M., Glover, B.J., Steiner, U.: J. Roc. Soc. Interface **7**, 1699 (2010)
71. Graham, R.M., Lee, D.W., Norstog, K.: Am. J. Bot. **80**, 198 (1993)
72. Gould, K.S., Lee, D.W.: Am. J. Bot. **83**, 45 (1996)
73. Lee, D.W.: Nature's Palette, the Science of Plant Colour. The University of Chicago Press, Chicago (2007)
74. Lee, D.W.: Nature **349**, 260 (1991)
75. Lee, D.W., Taylor, G.T., Irvine, A.K.: Int. J. Plant Sci. **161**, 297 (2000)
76. Richards, P.W.: The Tropical Rainforest, 2nd edn. Cambridge University Press, London (1994)
77. Neville, A.C.: J. Insect Physiol. **23**, 1267 (1977)
78. Steinbrecht, R.A., Mohren, W., Pulker, H.K., Schneider, D.: Proc. R. Soc. Lond. B **226**, 367 (1985)
79. Steinbrecht, R.A.: Tissue Cell **17**, 745 (1985)
80. Parker, A.R.: J. Exp. Biol. **201**, 2343 (1998)
81. Campos-Fernández, C., Azofeifa, D.E., Hernández-Jiménez, M., Ruiz-Ruiz, A., Vargas, W.E.: Opt. Mater. Express **1**, 85 (2011)
82. Bouligand, Y.: C. R. Acad. Sci. Paris **261**, 4864 (1965)
83. Neville, A.C., Caveney, S.: Biol. Rev. Cambridge Philos. Soc. **44**, 531 (1969)
84. Caveney, S.: Proc. R. Soc. Lond. B **178**, 205 (1971)
85. Neville, A.C.: Biology of the Arthropod Cuticle. Springer, Berlin (1975)
86. Neville, A.C., Parry, D.A.D., Woodhead-Galloway, J.: J. Cell Sci. **21**, 73 (1976)
87. Bouligand, Y.: In: Bruter, C.P., Arangol, A., Lichenrowicz, A. (eds.) Bifurcation Theory, Mechanics, and Physics. Riedel, Dordecht (1983)
88. Neville, A.C.: Biology of Fibrous Composites Development Beyond the Membrane. Cambridge University Press, Cambridge (1993)
89. Osorio, D., Ham, A.D.: J. Exp. Biol. **205**, 2017 (2002)
90. Goldstein, D.H.: Appl. Opt. **45**, 7944 (2006).
91. Bouligand, Y.: C. R. Chim. **11**, 281 (2008)
92. Sharma, V., Crne, M., Park, J.O., Srinivasarao, M.: Science **325**, 449 (2009)
93. Schultz, T.D., Rankin, M.A.: J. Exp. Biol. **117**, 87 (1985)
94. Schultz, T.D.: Bull. Entomol. Soc. Am. **32**, 142 (1986)
95. Schultz, T.D., Bernard, G.D.: Nature **337**, 72 (1989)
96. Liu, F., Yin, H.W., Dong, B.Q., Qing, Y.H., Zhao, L., Meyer, S., Liu, X.H., Zi, J., Chen, B.: Phys. Rev. E **77**, 012901 (2008)
97. Vukusic, P., Sambles, J.R., Lawrence, C.R.: Nature (London) **404**, 457 (2000)
98. Yoshioka, S., Kinoshita, S.: Opt. Express **15**, 2691 (2007)
99. Yoshioka, S., Kinoshita, S.: J. R. Soc. Interface **5**, 457 (2007)
100. Loewen, E.G., Popov, E.: Diffraction Gratings and Applications. Marcel Dekker, New York (1997)
101. Hinton, H.E.: Entomologist **102**, 185 (1969)
102. Hinton, H.E., Gibbs, D.: Nature **221**, 953 (1969)
103. Hinton, H.E., Gibbs, D.: J. Insect Physiol. **15**, 959 (1969)
104. Hinton, H.E., Gibbs, D.: J. Insect Physiol. **17**, 1023 (1971)
105. Hinton, H.E.: Some little known surface structures. In: Neville, A.C. (ed.) Insect Ultrastructure, pp. 41–58. Royal Entomological Society, London (1973)
106. Hinton, H.E.: Natural deception. In: Gregory, R.L., Gombrich, E.H. (eds.) Illusion in Nature and Art, pp. 97–159. Duckworth, London (1973)

107. Hinton, H.E.: Proc. Br. Ent. Nat. Hist. Soc. **6**, 43 (1973)
108. Seago, A.E., Wheeler, Q.D.: Coleopterists Bull. **58**, 235 (2004)
109. Ingram, A.L., Lousse, V., Parker, A.R., Vigneron, J.P.: J. Roc. Soc. Interface **5**, 1387 (2008)
110. Parker, A.R.: Proc. Roc. Soc. Lond. B **262**, 349 (1995)
111. Whitney, H.M., Kolle, M., Andrew, P., Chittka, L., Steiner, U., Glover, B.J.: Science **323**, 130 (2009)
112. Whitney, H.M., Kolle, M., Alvarez-Fernandez, R., Steiner, U., Glover, B.J.: Communicative Integr. Biol. **2**, 230 (2009)
113. Vigneron, J.P., Rassart, M., Vertesy, Z., Kertesz, K., Sarrazin, M.L., Biro, L.P., Ertz, D., Lousse, V.: Phys. Rev. E **71**, 011906 (2005)
114. Miller, W.H., Moller, A.R., Bernhard, C.G.: The corneal nipple array. In: Bernhard, C.G. (ed.) The Functional Organisation of the Compound Eye, p. 21. Pergamon, Oxford (1966)
115. Miller, W.H., Bernard, G.D., Allen, J.L.: Science **162**, 760 (1968)
116. Parker, A.R., Hegedus, Z., Watts, R.A.: Proc. Roc. Soc. Lond. B **265**, 811 (1998)
117. Stavenga, D.G., Foletti, S., Palasantzas, G., Arikawa, K.: Proc. Roc. Soc. Lond. B **273**, 661 (2006)
118. Yoshida, A., Motoyama, M., Kosaku, A., Miyamoto, K.: Zool. Sci. **13**, 525 (1996)
119. Binetti, V.R., Schiffman, J.D., Leaffer, O.D., Spanier, J.E., Schauer, C.L.: Integr. Biol. **1**, 324 (2009)
120. Parker, A.R., McPhedran, R.C., McKenzie, D.R., Botten, L.C., Nicorovici, N.A.: Nature **409**, 36 (2001)
121. Prum, R.O., Torres, R.: J. Exp. Biol. **206**, 2409 (2003)
122. Durrer, H.: Verhand. Naturforsch. Ges. Basel **73**, 204 (1962)
123. Yoshioka, S., Kinoshita, S.: Forma **17**, 169 (2002)
124. Zi, J., Yu, X.D., Li, Y.Z., Hu, X.H., Xu, C., Wang, X.J., Liu, X.H., Fu, R.T.: Proc. Natl. Acad. Sci. USA **100**, 12576 (2003)
125. Li, Y.Z., Lu, Z.H., Yin, H.W., Yu, X.D., Liu, X.H., Zi, J.: Phys. Rev. E **72**, 010902(R) (2005)
126. Parker, A.R., Welch, V.L., Driver, D., Martini, N.: Nature **426**, 786 (2003)
127. Maldovan, M., Thomas, E.L.: Nat. Mater. **3**, 593 (2004)
128. Galusha, J.W., Richey, L.R., Gardner, J.S., Cha, J.N., Bartl, M.H.: Phys. Rev. E **77**, 050904(R) (2008)
129. Morris, R.B.: J. Entomol. A **49**, 149 (1975)
130. Ghiradella, H., Radigan, W.: J. Morphol. **150**, 279 (1976)
131. Ghiradella, H.: J. Morphol. **202**, 69 (1989)
132. Argyros, A., Large, M.C.J., McKenzie, D.R., Cox G.C., Dwarte, D.M.: Micron **33**, 483 (2002)
133. Prum, R.O., Quinn, T., Torres, R.H.: J. Exp. Biol. **209**, 748 (2006)
134. Kertész, K., Bálint, Z., Vértesy, Z., Márk, G.I., Lousse, V., Vigneron, J.P., Rassart, M., Biró, L.P.: Phys. Rev. E **74**, 021922 (2006)
135. Michielsen, K., Stavenga, D.G.: J. R. Soc. Interface **5**, 85 (2008)
136. Michielsen, K., De Raedt, H., Stavenga, D.G.: J. R. Soc. Interface **7**, 765 (2010)
137. Saranathan, V., Osuji, C.O., Mochrie, S.G.J., Noh, H., Narayanan, S., Sandy, A., Dufresne, E.R., Prum, R.O.: Proc. Natl. Acad. Sci. USA **107**, 11676 (2010)
138. Häcker, V., Meyer, G.: Zool. Jb. Abt. Syst. Geog. Biol. Tiere **15**, 267 (1902)
139. Finger, E.: Naturwissenschaften **82**, 570 (1995)
140. Raman, C.V.: Proc. Ind. Acad. Sci. A **1**, 1 (1934)
141. Dyck, J.: Z. Zellforsch. **115**, 17 (1971)
142. Dyck, J.: In: Proc. Int. Orthnithol. Congr., vol. 16, p. 426. Australian Acad. Sci., Canberra (1976)
143. Prum, R.O., Torres, R.H., Williamson, S., Dyck, J.: Nature **396**, 28 (1998)
144. Prum, R.O., Torres, R., Williamson, S., Dyck, J.: Proc. R. Soc. Lond. B **266**, 13 (1999)
145. Dufresne, E.R., Noh, H., Saranathan, V., Mochrie, S.G.J., Cao, H., Prum, R.O.: Soft Matter **5**, 1792 (2009)
146. Noh, H., Liew, S.F., Saranathan, V., Mochrie, S.G.J., Prum, R.O., Dufresne, E.R., Cao, H.: Adv. Mater. **22**, 2871 (2010)

147. Shawkey, M.D., Estes, A.M., Siefferman, L.M., Hill, G.E.: Proc. R. Soc. Lond. B **270**, 1455 (2003)
148. Dong, B.Q., Liu, X.H., Zhan, T.R., Jiang, L.P., Yin, H.W., Liu, F., Zi, J.: Opt. Express **18**, 14430 (2010)
149. Dong, B.Q., Zhan, T.R., Liu, X.H., Jiang, L.P., Liu, F., Hu, X.H., Zi, J.: Phys. Rev. E **84**, 011915 (2011)
150. Prum, R.O., Torres, R., Kovach, C., Williamson, S., Goodman, S.M.: J. Exp. Biol. **202**, 3507 (1999)
151. Galusha, J.W., Richey, L.R., Jorgensen, M.R., Gardner, J.S., Bartl, M.H.: J. Mater. Chem. **20**, 1277 (2010)
152. Lafait, J., Andraud, C., Berthier, S., Boulenguez, J., Callet, P., Dumazet, S., Rassart, M., Vigneron, J.-P.: Mater. Sci. Eng. B **169**, 16 (2010)
153. Doucet, S.M., Shawkey, M.D., Rathburn, M.K., Mays Jr., H.L., Montgomerie, R.: Proc. R. Soc. Lond. B **271**, 1663 (2004)
154. Wickham, S., Large, M.C.J., Poladian, L., Jermiin, L.S.: J. R. Soc. Interface **3**, 99 (2006)
155. Parker, A.R.: Phil. Trans. R. Soc. B **363**, 2465 (2008)
156. Hubbard, J.K., Uy, J.A.C., Hauber, M.E., Hoekstra, H.E., Safran, R.J.: Trends Genet. **26**, 231 (2010)
157. Doucet, S.M., Meadows, M.G.: J. R. Soc. Interface **6**, S115 (2009)
158. Biró, L.P., Bálint, Zs., Kertész, K., Vértesy, Z., Márk, G.I., Horváth, Z.E., Balázs, J., Méhn, D., Kiricsi, I., Lousse, V., Vigneron, J.P.: Phys. Rev. E **67**, 021907 (2003)
159. Jackson, A.P., Vincent, J.F.V., Turner, R.M.: Proc. R. Soc. Lond. B **234**, 415 (1988)
160. Butler, M.W., Johnson, A.S.: J. Exp. Biol. **207**, 285 (2004)
161. Gower, D.J.: J. Morphol. **258**, 249 (2003)
162. Douglas, R.H., Marshall, N.J.: In: Archer, S.N., Djamgoz, M.B.A., Loew, E.R., Partridge, J.C., Vallerga, S. (eds.) Adaptive Mechanisms in the Ecology of Vision, p. 95. Springer, New York (1999)
163. Parker, A.R.: Phil. Trans. R. Soc. A **364**, 1759 (2009)
164. Vukusic, P.: Contact Lens Spectrum **25**, 6 (2010)
165. Biró, L.P., Vigneron, J.P.: Laser Photon. Rev. **5**, 27 (2011).
166. Liu, K.S., Jiang, L.: Nano Today **6**, 155 (2011)